www.sciencemag.org/cgi/content/full/science.aah6765/DC1

Supplementary Materials for

Extensive water ice within Ceres' aqueously altered regolith: Evidence from nuclear spectroscopy

T. H. Prettyman,* N. Yamashita, M. J. Toplis, H. Y. McSween, N. Schorghofer, S. Marchi, W. C. Feldman, J. Castillo-Rogez, O. Forni, D. J. Lawrence, E. Ammannito, B. L. Ehlmann, H. G. Sizemore, S. P. Joy, C. A. Polanskey, M. D. Rayman, C. A. Raymond, C. T. Russell

*Corresponding author. Email: prettyman@psi.edu

Published 15 December 2016 on *Science* First Release
DOI: 10.1126/science.aah6765

This PDF file includes:

Contents

Materials and Methods

Instrument overview

Dawn's Gamma Ray and Neutron Detector (GRaND) is described by (*9*). For completeness, we provide an overview of the instrument and specific data products used in our analyses.

GRaND's design is based on the Lunar Prospector Gamma Ray Spectrometer (*27*), which was boom mounted to reduce spacecraft background. GRaND consists of a large-volume bismuth germanate (BGO) scintillator, surrounded by an anti-coincidence shield (ACS), which also serves as the neutron spectrometer (Fig. S1). GRaND is deck mounted. Consequently, the ACS was segmented to aid in separation of spacecraft and asteroid contributions (Fig. S1). The ACS consists of four scintillators: two phosphor sandwiches (phoswiches) located on the ±Z sides of the BGO ($Bi_4Ge_3O_{12}$) scintillator, and two boron-loaded plastic (BLP) scintillators on the ±Y sides. The BLP scintillators also wrap around the BGO scintillator on the –X side, and photomultiplier tubes are positioned on the +X side (*9*). An array of cadmium zinc telluride (CZT) semiconductor radiation detectors – a technology demonstration on Dawn – is located between the BGO and +Z phoswich.

The BGO scintillator is GRaND's primary gamma ray detector. Large volume (293 cm^3), high density (7.13 g/cm^3) (*28*), and high atomic number result in high efficiency for gamma ray detection. The BGO scintillator measures gamma rays from a few hundred keV to about 10 MeV with pulse height resolution of about 10% full-width-at-half-maximum (FWHM) at 0.662 MeV.

The +Z phoswich, which is pointed towards Ceres during science data acquisition, is GRaND's primary neutron spectrometer. The phoswich consists of a lithium-loaded glass (LiG) scintillator optically coupled to a block of BLP.

Neutrons in the thermal and epithermal energy range can be absorbed by ^6Li via the $^6Li(n,\alpha)t$ reaction (Figs. S1 and S2). Deposition of energy by the reaction products results in the production of sensible light, which makes a broad peak in the pulse height spectrum centered at about 260 keV_{ee} (Fig. S3). Here, "ee" denotes "electron equivalent" energy. That is to say, the ^6Li reaction makes the same average pulse amplitude as full energy deposition by a 260 keV electron.

The BLP scintillator is shielded from thermal neutrons by a Gd foil and the lithium-loaded glass. Neutrons in the epithermal range ($0.5\ eV < E_n < 0.5\ MeV$, where E_n is neutron kinetic energy) can be absorbed by the ^{10}B via the $^{10}B(n,\alpha)$ reaction, which results in a peak at 93 keV_{ee} (Figs. S1 and S2). For $E_n > 0.5$ MeV, light is efficiently made by protons recoiling from neutron elastic collisions with H. Neutrons that remain within the BLP are ultimately captured by ^{10}B, producing a second flash of light. Thus, a characteristic double pulse identifies fast neutrons (Fig. S2).

Galactic cosmic ray (GCR) interactions, such as the proton "punch through" event depicted in Fig. S1, result in simultaneous light output from multiple sensors. GRaND's triple coincidence counter records events in which three or more sensors are triggered. The triples counter is a proxy for long term variations in the flux of GCRs (*9*) and is used to compare relative production rates of gamma rays and neutrons between different periods of time.

Summary of data acquired at Ceres

GRaND powered on in March of 2015 as Dawn approached Ceres (see timeline, Fig. S4). The instrument was nominal throughout Ceres encounter, with the same suite of operational sensors used at Vesta. Neutrons and gamma rays from Ceres were detected as Dawn transitioned to high altitude mapping orbit (HAMO). During the primary mission, GRaND acquired data in a circular, polar low altitude mapping orbit (LAMO) from December of 2015 through 19-June. The data from the primary mission were archived at the Planetary Data System Small Bodies Node and can be accessed online (*29, 30*). The archive contains a time series of raw and calibrated data. Spacecraft ephemerides, pointing, and measurement geometry (solid angle) are provided for each science data record.

Prior to HAMO, instrument high voltage (HV) settings were optimized to ensure that reaction peaks and gamma rays were on scale. All scintillators had small, but noticeable losses in gain (about 10%), probably due to accumulation of radiation damage during the transfer from Vesta to Ceres. To compensate for these losses, the +Z phoswich HV was adjusted to 185 data number (DN) (1088 V), the same setting used in Vesta LAMO Epoch II (*11*). The BGO HV was adjusted to 127 DN (747 V), in comparison to 125 DN (735 V) used in all previous mission phases.

LAMO data analyzed in this study were accumulated over 5 months, between 16-Dec and 11-May, with negligible data loss. A total of 90,714 science data records (SDRs) were acquired, each with an accumulation interval (TELREADOUT) of 140s. During each interval, Dawn traversed about 2.5° of arc length along its orbit. For mapping and analyses, data that did not meet pointing criteria were discarded (Fig. S5), leaving 66,427 SDRs (73% duty cycle).

In comparison to Vesta, the measurement geometry was very consistent, given Ceres' relatively round shape and Dawn's nearly circular orbits (Fig. S6). The distance to the surface in the direction of body center ranged from 353- to 415-km, with a mean of 385 km and population standard deviation of 13 km. The solid angle subtended by Ceres at the spacecraft was calculated at each orbital location using a shape model determined via stereophotoclinometry with images acquired in HAMO (Fig. S7A). The shape model accompanies a time series of spacecraft ephemerides, pointing, and solid angles online (*30*). The solid angle ranged from 1.012- to 1.101-steradians (sr), with a mean of 1.057 sr and (population) standard deviation of 0.020 sr. In comparison, the range for Vesta LAMO was 0.880- to 1.297-sr, with a mean of 1.069 sr and a (population) standard deviation of 0.092 sr. The range of solid angles at Ceres (8% variation) is narrow compared to Vesta (nearly 40% variation); although, the averages are similar.

Dawn's encounters with Vesta and Ceres occurred, respectively, before and after a very weak solar maximum. Relatively few large solar energetic particle events were observed by GRaND at Ceres, and none were observed while in LAMO. This assessment is based on examination of the +Z phoswich time series (Figs. S4 and S5), which is sensitive to solar energetic particles. The GCR (triples) monitor gradually increased during LAMO and throughout Ceres encounter, consistent with decreasing solar activity (Fig. S7B).

Data reduction and mapping

A time series of net peak areas (counts/s) was determined for the following signatures (Fig. S8):

- ^{6}Li(n,α) reaction peak at 260 keV$_{ee}$, a single interaction with the +Z LiG scintillator, sensitive to neutrons in the thermal and epithermal energy ranges ("thermal + epithermal");
- ^{10}B(n,α) reaction peak at 93 keV$_{ee}$, a single pulse from the +Z BLP scintillator, sensitive to neutrons in the epithermal energy range;
- Full energy deposition of 7.6 MeV ^{56}Fe(n,γ) capture gamma rays, a single pulse from BGO;
- ^{10}B(n,α) second interaction peak at 93 keV$_{ee}$, a double-pulse in the +Z BLP scintillator, sensitive to neutrons in the fast energy range.

For fast neutrons, the time-to-second-pulse spectrum was filtered using a modified early time window (4- to 9-μs) (*9*) to eliminate spurious events that appear at earlier times (*31*). The area of the ^{10}B(n,α) reaction peak that appears in the second event pulse height spectrum is proportional to the fast neutron interaction rate (Fig. S8D).

Peak areas were determined from spectra summed over successive accumulation intervals, to produce a 3-point central moving average of net counts. Peak extraction methods for low resolution spectroscopy are described by (*9*). For each spectral sum, net counts were determined by subtracting continuum counts from a region of interest (ROI) containing the peak. The continuum counts within the peak ROI were determined by scaling a continuum shape function to match sum counts in one or more background ROIs. The following methods were used to determine the continuum shape function (Fig. S8):

- ^{6}Li(n,α) reaction peak: the +Z phoswich single-pulse spectrum measured far from Ceres;
- ^{10}B(n,α) reaction peak: a power law fitted to background channels above and below the peak for difference spectra (Fig. S3) summed over 101 measurements, a central moving average;
- 7.6 MeV ^{56}Fe(n,γ) capture peak: an exponential with pulse height fitted to the high energy continuum averaged over all LAMO measurements that met pointing criteria (cf. *32*);
- ^{10}B(n,α) second interaction peak: the +Z phoswich second event spectrum measured far from Ceres.

To remove geometric variations, net peak areas were divided by the solid angle subtended by Ceres by the spacecraft at their respective measurement locations. The net areas were then multiplied by a correction factor to account for variations in neutron and gamma ray production by GCRs.

The GCR correction factor was derived from the time series of solid-angle-corrected net areas for the ^{6}Li(n,α) reaction peak. The correction is based on methods developed for mapping data acquired by the 2001 Mars Odyssey Neutron Spectrometer (*33*). In the absence of variability in the GCR flux and temporal changes in surface composition, the counts measured over a selected spatial region should be the same from orbit to orbit. The average net counting rate within an equatorial band (30° of the equator) was determined in a contiguous, 491-point sliding window (3.5 orbits, roughly

20 hours) for each point in the time series. Application of the correction factor to the ^{6}Li(n,α) time series is illustrated in Fig. S9. The corrections are robust to the selection of the spatial region and averaging window.

Dawn's circular polar mapping orbit enabled full global coverage of Ceres (Fig. S10). Corrected, time series counting data were averaged within 20° quasi-equal-area pixels. Maps of counting data are displayed in Fig. 1 and Fig. S11. Due to the very low signal-to-background ratio (1:50) of the ^{10}B(n,α) peak, the epithermal signature was not used in this study for quantitative analyses of Ceres composition; however, the reduction in the intensity of this peak relative to Vesta (Fig. S3) indicates that Ceres is hydrogen rich and the spatial variation (Fig. S11) is consistent with higher concentrations of hydrogen near the poles than at the equator.

Simulation of neutron and gamma ray leakage currents

The interaction of GCRs with regolith materials on Ceres' surface was modeled using the Monte Carlo N-Particle eXtended (MCNPX) code (*34, 35*). MCNPX version 2.7.0 is available from the Radiation Safety Information Computational Center (*36*). MCNPX is widely used for planetary nuclear spectroscopy (e.g. *35, 37-40*). The collision of high-energy GCR ions with nuclei in the regolith makes secondary particles via spallation and evaporation. These undergo further interactions, producing particle shower that includes gamma rays and neutrons, some of which escape into space. We used MCNPX to calculate the current of gamma rays and neutrons escaping from Ceres' surface. The current is the rate at which particles cross the surface into space.

Input parameters, including cross sections and physics models, were similar to those used for studies of Vesta (*11, 40*). Ceres was modeled as a homogeneous, equivalent-volume sphere, with an inner shell representing the ice table. The sphere was exposed to an isotropic flux of GCR protons and helium ions. The GCR differential flux was generated using the Badhwar - O'Neill model (2011 update) (*41, 42*), which solves the Fokker-Planck equation describing the drift/diffusion of GCR ions within the heliosphere. Since GRaND measurements were empirically corrected for temporal variations in the flux of galactic cosmic rays, the same GCR input spectrum, with a modulation potential of 550 MV (cf. *35, 40*), was used for all MCNPX simulations. Normalized counting rates reported here are insensitive to GCR spectral shape, which is controlled by the modulation potential. Using MCNPX, the leakage current of neutrons and gamma rays was tallied as a function of energy and angle. The source units were selected so that the current tallied by MCNPX had units of particles/s (e.g. *35*). The tally was converted to units of particles/cm^2/s/MeV/steradian by dividing by the surface area of Ceres, and the width of the energy- and angle bins. The calculations were carried out for representative regolith compositions and hydrogen layering.

Forward model of Counts (Figs. 2 and 3)

Simulated counting rates for the Fe 7.6 MeV gamma ray and thermal+epithermal neutrons are displayed on a relative scale in Fig. 2. To make Fig. 2, the simulated 7.6 MeV peak area was assumed to be proportional to the leakage current of 7.6 MeV gamma rays simulated by MCNPX. For neutrons, the leakage current was propagated to the

orbiting spectrometer using a physical model that accounts for neutron decay and detection, given the energy-angle response function of the phoswich. The model was used to simulate the response for surfaces with uniform composition within the field of view of the detector (Fig. 2) and heterogeneous surfaces, accounting for blurring of surface regions by the broad spatial response of the instrument (Fig. 3C). Model calculations were based on the ray tracing algorithm used to calculate the solid angle of Vesta and Ceres at different orbital locations using polygonal shape models (*43*).

The solid angle subtended by Ceres at the spacecraft is given by the following surface integral (e.g. *44*):

$$\Omega = \int_S dA \frac{\hat{n} \cdot \hat{\Omega}}{r^2} \tag{1}$$

where S is the set of all points on the surface visible from the spacecraft, $\hat{n}$ is the unit outward normal of the surface at a surface location, and $\hat{\Omega}$ and r are, respectively, the direction and distance from that surface location to the spacecraft. This integral can be solved using Monte Carlo (e.g. *43*): Rays originating from the spacecraft are selected randomly from an isotropic distribution. Rays that intersect Ceres, which is represented by a polygonal shape model, receive a score (*W*) of 1. Those that don't receive a score of zero. The fractional solid angle (out of 4π) is given by the ratio of the total score and the number of rays sampled.

The flux of neutrons at the detector (neutrons/cm^2/s) is given by an integral similar to Eq. 1:

$$\varphi(E) = \kappa \int_S dA \frac{j\left(\vec{r}, E, \hat{n} \cdot \hat{\Omega}\right) e^{-t/\tau}}{r^2} \tag{2}$$

where κ is a constant, $j\left(\vec{r}, E, \hat{n} \cdot \hat{\Omega}\right)$ is the leakage current of particles with energy E at location $\vec{r}$ on the surface of Ceres, determined by MCNPX, with units of particles/cm^2/s/steradian. The exponential term accounts for the decay of low energy neutrons for which the transit time to orbit t is comparable to the neutron lifetime τ. This formulation assumes that the neutrons travel in straight-line trajectories. Gravitational binding of neutrons is ignored (*40*).

The integral in Eq. 2 can be calculated by importance sampling (*45*) using the same ray-tracing algorithm used to calculate the solid angle; however, instead of scoring 1 when a ray strikes the shape model, the following weight is scored:

$$W = \frac{j\left(\vec{r}, E, \hat{n} \cdot \hat{\Omega}\right) e^{-t/\tau}}{\hat{n} \cdot \hat{\Omega}} \tag{3}$$

The weight is proportional to the ratio of the (actual) neutron emission distribution determined by MCNPX to the sampled (arbitrary) emission distribution, which varies linearly in the cosine of the emission angle (Eq. 1). A similar approach was used to

simulate the response of GRaND as Dawn flew by Mars (*9*). The weight can be further multiplied by the energy-dependent, efficiency-area product of the detector, which varies linearly with the angle of incidence (*9*), in which case the integral has units of counts/s.

The Monte Carlo integration algorithm was used to calculate the orbital response of GRaND (counts/s) for surfaces with spatially non-uniform compositions (ice table simulations shown in Fig. 3), accounting for spatial mixing of surface regions by GRaND's broad footprint. For convex bodies like Ceres, the radiation output from separate surface parcels is independent (decoupled). Consequently, surface leakage currents calculated for a uniform sphere by MCNPX for selected compositions were assigned to different surface regions to model heterogeneous surface composition.

Model compositions used in MCNPX simulations

The response of GRaND was calculated for selected solar system materials, including whole-rock compositions compiled for howardites (*40*, *46*), average compositions for carbonaceous- and ordinary-chondrites (*23*), and dust from Halley's comet (*47*). In addition, simulated (artificial) materials with variable Fe-content were extrapolated from CM and CI compositions to fill the gap in Fe concentration between CI and Halley's dust (Table S1). For each material, hydration trends were modeled by removing all H as H_2O, and mixing H_2O with the H-free composition to achieve the desired water-equivalent hydrogen (WEH) content. For hydrogen layering, the regolith was modeled as two, homogeneous layers, guided by ice stability modeling (e.g. *13*). For selected compositions, we modeled permutations on the WEH concentration of the upper (W_{up}) and lower layer (W_{dn}) and depth of the lower layer (D), with $W_{up} \leq W_{dn}$ (see Fig. 2) (*33*, *48*). For the latitude profiles shown in Fig. 3B, Ceres' ice-free composition was assumed to be spatially uniform. Only spatial variations in depth (D) were modeled.

Ice retreat model

As water ice near the surface sublimates, the molecules diffuse through the porous subsurface, and are lost to space. An ice retreat model quantifies the gradual loss of water to space over 4.5 Gyr since Ceres' formation, based on subsurface temperatures and the physical properties of the overlying layer. The increase in solar luminosity over time is taken into account.

The model calculations are initialized with a mixture of ice and dust and assume a thermal inertia for the ice-free material of 15 $Jm^{-2}K^{-1}s^{-1/2}$, the best measurement from Earth-based observatories (*49*), and a grain density of 2.5 g/cm^3. The particle size in the surface layer is varied, but must be small ($\lesssim$100 μm) to be consistent with the low thermal inertia. The particle size determines the size of the pores and sets the vapor diffusion coefficient. Other than due to impact gardening, ice recedes with a sharply defined ice table, giving rise to a two-layered structure, with an ice-free upper layer and an ice-rich lower layer. In all model results included here, the porosity initially equals the volumetric ice-fraction, i.e. the pore spaces are initially completely filled with ice. Model calculations with impact gardening, similar to lunar rates and represented as stochastic mixing of the upper regolith, show erosion of the ice table, but overall only a minor modification of the depth-to-ice (*13*).

The first model calculations of the desiccation of an ice-rich crust on Ceres were carried out by Fanale & Salvail (*6*). The most significant difference to their model is the incorporation of diurnal temperature variations (i.e. much smaller time steps). Large surface temperature oscillations lead to colder temperatures at depth, due to the nonlinearity of the Stefan-Boltzmann radiation law, and thus to less ice loss and shallower burial depths. For example, the equatorial mean (i.e. time-averaged) surface temperature in the model is about 154K, as compared to 180K in Fanale & Salvail. Other models have predicted the stability of ice on Ceres using a 'buried snow line temperature' (*50, 51*).

Proper (not current) orbital elements are used, as these represent the long-term average, and the solar longitude of perihelion is allowed to precess, which leads to hemispherically symmetric depths-to-ice. Although southern summer currently occurs near perihelion, the orbit as well as the spin axis precess, at periods of 24 kyr and 22 kyr respectively (*52*), and no hemispheric asymmetry in the long-term average insolation (incoming solar radiation) is expected. Since the current depth of the ice is the cumulative result of 4.5 Gyr of retreat, the most recent precession cycle added only a tiny fraction to these depths. Other details of the model are described elsewhere (*13, 53*), and the source code is available online (*54*). A suite of model calculations has been carried out for comparison with GRaND results, with a range of particle sizes, porosities (ice fractions), and with and without impact gardening.

Model calculations for three cases with impact gardening are shown in Fig. 3B:

- Case a - low diffusivity, with a grain size of 1 μm and porosity of 0.1 (4 wt.% water ice);
- Case b - high diffusivity, with a grain size of 10 μm and porosity of 0.5 (30 wt.% water ice);
- Case c - low diffusivity, with a grain size of 1 μm and porosity of 0.2 (10 wt.% water ice).

Comparison of Vesta, Ceres and models (Fig. 2)

In Fig. 2, measurements of Ceres were plotted on a relative scale with Vesta and simulated counting rates for different model compositions. For each signature, the map data were normalized to their global, sample weighted average and then multiplied by the ratio of orbit-averaged counting rates measured in LAMO (Ceres/Vesta). In forming this ratio, the vestan rates were corrected to the cerean measurement geometry by multiplying by the ratio of LAMO average solid angles. The vestan rates were further adjusted to remove differences in GCR production rates by multiplying by the ratio of LAMO average triples rates, corrected for "shadowing" effects (*9*).

The globally-averaged Ceres/Vesta counting ratios were 0.32 ± 0.02 for $^{6}Li(n,\alpha)$ reaction and 1.48 ± 0.06 for the 7.6 MeV gamma ray. Statistical variations in globally-averaged spectra contribute negligibly to the uncertainty the ratios. The quoted errors are estimates of the systematic uncertainty in determining net peak areas using different methods, baseline subtraction (Fig. S8) and peak fitting (e.g. Fig. S17), and parameter variations (e.g., boundaries for regions of interest). In the following discussion, we show how assumptions regarding Vesta's global composition influence interpretation of Ceres' composition. Uncertainties in the Ceres/Vesta counting ratios are not considered;

however, they do affect the uncertainty in the [H] and [Fe] determined for Ceres' non-icy regolith [see Concentrations of H and Fe in Ceres ice-free regolith (Fig. 4)].

Placement of the normalized counting data on the same relative scale as the models requires knowledge of Vesta's mean regolith composition, which is not precisely known. However, a lower bound on Vesta's global average [H] (250 μg/g) was determined by the analysis of GRaND data (*11*), and the howardite meteorites, which are primarily a mixture of basaltic eucrite and diogenite, are thought to be representative of Vesta's regolith (e.g. *46*).

Globally-averaged counting rates for Vesta were modeled for different combinations of assumed values for Vesta's global average [H] and model compositions for Vesta's H-free regolith, obtained by varying the percentage of eucritic material in howardite (*40*). Experimental counting ratios (Ceres' pixel counting rates normalized to Vesta's global average) were normalized to the model counting rates for Vesta. In order to determine the sensitivity of assumptions about Vesta's composition, the following cases were considered:

1. *Minimum*: Vesta's global regolith is modeled as howardite with 55% basaltic eucrite, with a global average [H] of 250 μg/g;
2. *Random*: Multiple random samples of Vesta's global average [H] and basaltic eucrite content.

For the minimum case, the counting rates for Vesta were plotted at (1,1) in Figs. 2 and S12. For random samples shown in Fig. S12, model counting rates for Vesta were plotted relative to (1,1). Random samples of [H] and basaltic eucrite content were selected from a two-dimensional normal distribution ([H] = 400 ± 200 μg/g; basaltic eucrite content = 60% ± 10%). The random points for Vesta are shown as an ellipse (95% confidence interval) and the corresponding Ceres data are shown as grey points in Fig. S12. The mean and standard deviation for [H] was arbitrarily selected to include the minimum [H] determined by GRaND. The random samples show that higher [H] within Vesta's regolith would push the Ceres map data closer to the hydration trend-line for the CI chondrite model composition.

In the main text, we adopt the minimum global [H] on Vesta as ground truth for determining the concentrations of H and Fe on Ceres. This assumption gives a robust lower bound on the H content of Ceres' ice-free regolith for comparison with meteorite analogs. In addition, the minimum is likely representative of Vesta's surface.

Among several hundred howardite meteorites (*55*), there are a few that show evidence for exposure on the surface of Vesta (*11, 56-58*). These regolithic howardites contain solar wind Ne and, in many cases, coarse carbonaceous chondrite clasts, exogenous material delivered to Vesta's basaltic crust. These samples are inferred to contain between 240- to 600-μg/g H (*11*) in the form of hydrated minerals in the carbonaceous chondrite clasts, consistent with 400 μg/g H measured by GRaND in Vesta's low-albedo hemisphere (*11*). Analysis of Ne in regolithic howardites indicates that the vestan regolith contains 1- to 100-μg/g H from the solar wind (*11*). The relatively young Rheasilvia impact basin (*59, 60*) contains the lowest concentrations of H and OH on Vesta (*11, 61*). If H within Rheasilvia was delivered primarily by the solar wind, then the 250 μg/g lower bound from GRaND is representative of the actual globally averaged [H] in Vesta's upper regolith.

Hydrogen mapping with thermal + epithermal neutrons (Figs. 3A)

Production, moderation and absorption control the population of neutrons within the regolith. The number of neutrons made by GCR interactions scales roughly with the average atomic mass of the regolith. Successive collisions with regolith nuclei moderates the energy of the neutrons. Fast neutrons undergo inelastic and elastic collisions. Slower neutrons in the epithermal and thermal energy ranges interact via elastic scattering. The cross section for neutron radiative capture – an important loss mechanism – approximately varies inversely with neutron speed.

The energy lost by neutrons in elastic collisions depends on the atomic mass of the target nuclei. Hydrogen is a powerful moderator. On average, neutrons lose half their energy per elastic collision with hydrogen (*62*). In comparison, neutrons lose an average of about 14% per collision with C and 11% with O. The addition of hydrogen to regolith materials results in more rapid energy loss, suppressing the flux in the fast and epithermal energy ranges. The addition of small amounts of hydrogen to a "dry" material results in an initial increase in the flux of neutrons approaching thermal equilibrium with the regolith; however, the increase is offset by absorption as more hydrogen is added.

Because neutrons in the epithermal energy range mainly undergo elastic collisions, the epithermal neutron leakage flux depends strongly on hydrogen content. For achondrites, hydrogen concentration can be determined reliably from epithermal neutrons (*11*); however, analogs for Ceres and primitive solar system materials are C-rich (Table S1) . Although C is 12 times more massive than H, C and other light elements can affect moderation in planetary crustal materials; however, for model materials, relative variations in C content are large. For these materials, changes in C content can have a noticeable effect on the neutron leakage flux.

For fixed [H], increasing C content results in a decrease in the average atomic mass of the regolith, which will result in decreased neutron production (Fig. S13A). The addition of C also increases the energy loss cross section, resulting in a suppression of the neutron flux in the epithermal energy range (Fig. S13B).

The neutron leakage spectra for C-poor L chondrite (2500 μg/g C) and C-rich Halley's dust (24 wt.% C), both with 7% WEH are compared in Fig. S14A. For the C-rich sample, the neutron population is suppressed in the epithermal range, while the leakage current of thermal neutrons is enhanced (*63*). Plots of relative neutron counts as a function of WEH show considerable variability as a function of [C] for epithermal and fast neutrons (Figs. S14B and S14C); however, the trends for thermal + epithermal counts are similar, due in part to the increase/decrease in the flux of thermal/epithermal neutrons when C is added. The trends converge with added water, which dilutes contributions from other elements. For [H] greater than 10 wt.% WEH, the [H] can be determined reliably from thermal + epithermal neutron measurements (lines terminating with arrow in Fig. S14D) with an uncertainty of 1 wt.% WEH (1σ) or less for the range of model compositions considered. For mapping relative variations in [H] (e.g. Fig. 3), this is the dominant source of error. Contributions from statistical variations in the mapped counting data (error bars in Fig. 1A) are small in comparison. We also found that the relative variation of [H] on Ceres does not depend strongly on assumptions regarding placement of counts on a relative scale with the models (i.e. assumptions regarding the H

content of Vesta's regolith and uncertainties in the Ceres/Vesta counting ratio). The uncertainty in estimates of the ice content based on the difference between equatorial and polar hydrogen concentrations (Fig. 3C) is about 1 wt.% WEH.

Modeling shows that thermal + epithermal counting rates are insensitive to the temperature of the regolith. Following (*64*), the neutron leakage current was calculated for representative materials at different regolith temperatures (70 K and 150 K). The thermal leakage current is sensitive to the temperature of the regolith just below the diurnal temperature wave (at depths of about 30 g/cm^2). Based on thermal modeling (this study), the equatorial temperature is predicted to be about 150 K at this depth; whereas, the temperature at the pole is about 70 K. For the range of model compositions, we found that thermal + epithemal rate decreased on average by 1% from 150 K to 70 K, with a maximum change of less than 2%. This variation has negligible influence on the determination of H content. Changes in regolith temperature cannot explain the nearly 30% latitude variation in thermal + epithermal counts observed at Ceres (Fig. 1A).

Determining Fe concentration

The hydration trends for model compositions (Table S1) form a grid, which can be used to determine [Fe] for equatorial pixels (Fig. S15). For each model composition, the 7.6 MeV interaction rate follows an arc with increasing [H] (equivalently, with decreasing thermal + epithermal rate). For low [H], the 7.6 MeV rate increases as water is added. Added H increases the flux of thermal neutrons, which results in an increase in the production of 7.6 MeV Fe capture gamma rays. For high [H] (greater than about 10%, depending on composition), the 7.6 MeV rate decreases, due to dilution of Fe by water and increased capture of thermal neutrons by H. For fixed thermal + epithermal rate (equivalently, [H]), the 7.6 MeV rate increases monotonically with increasing [Fe]. The [Fe] for measured 7.6 MeV rates can be determined by linear interpolation of the model values along a vertical transect through the grid as shown in Fig. S15.

Concentrations of H and Fe in Ceres ice-free regolith (Fig. 4)

The [H] and [Fe] plotted in Fig. 4 was determined using the methods described above for different assumed values for the global average [H] of Vesta's regolith, ranging from 250 μg/g H (black diamond) to 800 μg/g (white diamond with blue outline). For each assumed value, the concentrations of H and Fe were determined from the mapped counting data (Fig. 1) for each of the 36, 20° quasi-equal-area pixels near the equator. The average of the equatorial pixels is shown in Fig. 4. The following sources of uncertainty were combined in quadrature to determine the error bars shown in Fig. 4, which indicates the dispersion of pixel values:

- The population standard deviation of the sampled pixels, approximately 0.4 wt.% WEH and 0.7 wt.% Fe;
- Systematic uncertainties in the Ceres/Vesta counting ratio, which was used to place the experimental data on a relative scale with models [see Comparison of Vesta, Ceres and models (Fig. 2)], corresponding to 1.7 wt.% WEH and 0.1 wt.% Fe;

- For H, an additional 1 wt.% WEH uncertainty in converting thermal + epithermal counting rates to H concentration was included [see Hydrogen mapping with thermal + epithermal neutrons (Figs. 3A)].

When combined, the total uncertainty was approximately 2 wt.% WEH and 1 wt.% Fe.

Gamma ray spectrum analysis

Pulse height spectra from the BGO scintillator acquired in LAMO include contributions from gamma rays produced within Ceres' regolith as well as by GCR interactions with the spacecraft. To eliminate spacecraft contributions, we subtracted a background spectrum accumulated over 29 days at great distance from Ceres (orbital radius > 3000 km, prior to 27-Jul) from spectra acquired in LAMO. The background accumulation period was selected so that the BGO HV setting matched that used for LAMO. The difference spectrum is sensitive to gamma rays originating from Ceres (Fig. S16). All spectra were divided by live-time and corrected for variations in gain and peak-width (*65*). Data that did not meet pointing criteria (Fig. S5) were excluded from spectral sums in LAMO.

The 7.6 MeV gamma ray from neutron capture with Fe, which is absent in the background spectrum appears prominently in the spectrum acquired at low altitude (Fig. S16). Prominent peaks from fast neutron interactions with C and O also appear in the spectrum above 4 MeV. At low energies, the difference spectrum contains a strong peak at about 2.2 MeV, which should include contributions from radiative neutron capture with H; however, this peak also contains unknown contributions from neutron interactions with Al and S. The 2.2 MeV peak is about 40% higher than observed at Vesta for which contributions are primarily from neutron inelastic scattering with Al (*11*). This is consistent with Ceres having a H-rich regolith; however, because the contributions from Al and S are unknown, the change in neutron counts relative to Vesta is a more robust measure of the H content of Ceres' regolith. In addition, a prominent peak appears at 1.78 MeV, which includes contributions from neutron inelastic scattering with Si. This peak is 25% the intensity measured at Vesta, which is consistent with Ceres having lower Si content than Vesta. This is not unexpected given that analog carbonaceous chondrite meteorites have lower Si content than howardite meteorites (*23*); however, quantification of Si is challenging due to unknown contributions from Al and Fe (e.g. neutron capture by Al at 1.779 MeV and inelastic neutron scattering with Fe at 1.810-MeV) (*66*). Consequently, gamma ray analyses of H and Si are not reported.

For the analysis of gamma rays produced by nuclear reactions, the background was weighted (*67*) prior to subtraction to account for changes in the flux of GCRs between the background measurement and LAMO (Fig. S16). The weighting algorithm simultaneously corrects for shadowing of the spacecraft by Ceres. The change in GCR flux was determined from the triples coincidence counter using methods described by (*67*). An unweighted ("straight") difference was used in the analysis of natural radioelements.

Regions of the gamma ray spectrum were fitted with Gaussian shapes, representing discrete gamma rays, and a power law, representing the continuum. The peak areas are proportional to the full energy interaction rates of characteristic gamma rays made by specific nuclear reactions.

Fig. S17A shows the low energy region of the "straight" difference spectrum (*64*), which contains the 1.46 MeV gamma ray from the decay of ^{40}K. For spectra acquired in the equatorial region within ±20° latitude, the net peak area was 0.045 ± 0.004 counts/s. The [K] is proportional to the 1.46 MeV peak area. The constant of proportionality depends on the half-life of ^{40}K, gamma ray yield, average solid angle of Ceres, and the efficiency of the BGO scintillator (*67*). The constant also depends weakly on the gamma ray mass attenuation coefficient of the regolith. We used the XCOM program (*68*) to calculate the mass attenuation coefficient of the model CI and CM chondrite compositions for the 34 most abundant elements in Table 1. The mass attenuation coefficients for CI and CM chondrites are 0.053- and 0.052 cm^2/g, respectively. Given the average solid angle of Ceres of 1.057 in LAMO and the average mass attenuation coefficient for CI and CM chondrites, the proportionality constant for Ceres was 9.12×10^3 μg/g/(counts/s) (Eq. 3 and Table A1 of *67*). This gives [K] of 410 ± 40 μg/g for Ceres' non-icy regolith.

At mid-high energies (>4 MeV), the weighted difference spectrum contains significant contributions from C, O and Fe (Fig. S17B). The prominent peak at 7.6 MeV, which does not appear in high altitude spectra (Fig. S16), is a gamma-ray doublet (7.631- and 7.646-MeV) produced by radiative neutron capture by ^{56}Fe within Ceres' regolith. The peak at 4.4 MeV contains contributions from C and O, including neutron inelastic scattering with ^{12}C (for neutrons with energies above the reaction threshold, E_n > 4.4 MeV), and spallation of ^{16}O (E_n > 15 MeV). Both reactions make the first excited state of ^{12}C, which de-excites by emission of a 4.438 MeV gamma ray (*66*). The peak at about 6.1 MeV contains unresolved contributions from Fe and O, which are separated by peak fitting. Neutron inelastic scattering with ^{16}O (E_n > 6.1 MeV) produces a 6.129 MeV gamma ray. The areas of peaks are given in Table S2.

The full energy peak intensity (net peak area in counts/s) for a gamma ray with energy E is proportional to the current of gamma rays escaping the surface, F_E (gamma-rays/cm^2/s), and the intrinsic efficiency ε_E of the BGO scintillator at that energy. Nuclear reactions with elements can produce gamma rays at multiple energies (*66*). The contribution of gamma rays produced by the same element to peaks in the gamma ray spectrum can be estimated if the peak area for one of the gamma rays is known (e.g. *11, 69*). The elemental contribution to a peak at energy E' is given by $A\times\left(F_{E'}/F_E\right)\times\left(\varepsilon_{E'}/\varepsilon_E\right)$, where A is the measured peak area (counts/s) for a single gamma ray with energy E. For nuclear reactions produced by the same reaction type (i.e. fast neutron inelastic scattering or neutron capture), the ratio of currents is roughly independent of regolith composition (*38, 70*).

Using this approach, contributions to the 4.4 MeV peak by spallation of ^{16}O were estimated from the peak area for the 6.1 MeV gamma ray made by neutron inelastic scattering with ^{16}O. The 6.1 MeV peak area was multiplied by the relative efficiency of the BGO scintillator ($\varepsilon_{4.4}/\varepsilon_{6.1}$ = 1.15) (*9*) and the ratio of the leakage current calculated by MCNPX for average CI chondrite ($F_{4.4}/F_{6.1}$ = 0.40). The ratio of currents is nearly identical to that calculated by (*63*) for average lunar soil ($F_{4.4}/F_{6.1}$ = 0.42). The estimated contribution from O (0.018 ± 0.001 counts/s) was subtracted from the area of the 4.4 MeV peak (C+O in Table S2) to determine the contribution of C to the 4.4 MeV peak (C in Table S2). The quoted uncertainties in Table S2 are propagated, statistical counting

errors. Systematic errors in the current- and efficiency-ratios should contribute <10% to the relative uncertainty in C counts (*9*).

Detection of carbon

The presence of high concentrations of C within Ceres' regolith can be tested by comparing GCR-corrected 4.4- and 6.1-MeV peak areas measured at Ceres and Vesta (Table S2). The production rate of gamma rays depends on the atom density of the target element and the flux of interrogating neutrons with energies greater than the reaction threshold. The 6.1-MeV interaction rate is about a factor of two lower at Ceres than at Vesta, consistent with a large observed decrease in the leakage flux of fast neutrons (Fig. S18). Vestan and cerean model compositions have similar O content. Therefore, the difference in counting rates is not likely due to changes in [O]. In contrast, the C contribution to the 4.4 MeV peak is over a factor of two higher at Ceres than at Vesta. Despite exogenic contamination by carbonaceous impactors, the C content of Vesta's regolith is small (< 0.1 wt.% if the H measured by GRaND was delivered by impactors with CM chondrite composition). Therefore, C contributions to the 4.4 MeV peak at Vesta must be caused by the interaction of neutrons made in Vesta's regolith with GRaND's carbon-composite housing. That the C contribution to 4.4 MeV peak increases at Ceres, despite a large reduction in the flux of interrogating fast neutrons, is evidence for elevated [C] in Ceres regolith. However, unknown backgrounds from neutrons impinging on GRaND's C-rich housing complicate quantification of [C] using gamma rays.

Equatorial fast and thermal + epithermal neutron counting rates (for pixels within 20° of the equator, representative of Ceres' ice-free regolith) plot close to the CI chondrite model rates (Fig. S18). The spread of equatorial fast neutron measurements overlaps the CI chondrite model. However, the average equatorial value for fast neutrons is about 3σ lower than the model, falling between the hydration lines for Halley's dust and CI chondrite. The shift to lower rates may result from moderation by C. If so, then Ceres' regolith may contain more C than CI chondrites (greater than a few %). The error bars are for precision only and systematic errors may contribute to the offset. For the chart shown in Fig. S18, the position of the data is insensitive to assumptions for minimum [H] on Vesta.

Hydrogen and Iron concentrations in meteorites (Fig. 4)

Fig. 4 shows published analyses of total Fe and H content, expressed as water-equivalent hydrogen (WEH = 9 × [H]), for selected CM and CI chondrites. The plotted values and references are listed in Table S3.

Measurements of indigenous H are challenging due to contamination of samples by terrestrial atmospheric water, which is readily adsorbed by phyllosilicates, as well as possible alteration of the meteorite during its passage through the atmosphere (*18*). Our compilation is based on recent results from mass spectrometry (*18, 71*) and thermogravimetric analysis (TGA) (*72*). Mass spectrometry provides a direct measurement of total H; whereas, with TGA, H_2O content is inferred from changes in the mass of the sample as it is heated. Both methods give similar results for CM chondrites;

however, for CI chondrites, TGA may overestimate water content since phases other than water may contribute to mass loss (*73*). For TGA analyses reported by (*72*), water content was taken to be the mass loss between 400- and 770-°C (cf. *73*). Table S3 includes published analyses of Fe for 17 meteorites. Four of these were assigned Fe concentrations from a paired meteorite (*18*).

Supplementary Text

Constraints on the mineralogy of Ceres

GRaND measurements of the concentration of Fe and H in Ceres' ice-free regolith differ from the aqueously altered carbonaceous chondrites. The concentration of H measured by GRaND (17 ± 2 wt.% WEH, equivalently 1.9 ± 0.2 wt.% H) is somewhat larger than for the CI chondrites. Measurements of Orgueil (CI1) by mass spectrometry give 1.56 wt.% H (*18*), within two standard deviations of the measurement by GRaND. For CI chondrites, H is in the form of phyllosilicates, including serpentine group minerals and clays, hydroxides and organic compounds (*74, 75*). Anhydrous species include magnetite and carbonates. Of the phyllosilicates, serpentine contains the highest H content (up to 1.4 wt.%). Dry clays such as montmorillonite contain less than 1 wt.% H as structural OH. Although adsorption of water can push the hydrogen content of clay minerals well above 2 wt.% in terrestrial settings, the presence of significant contributions from adsorbed water in Ceres' upper regolith seems unlikely given the low water vapor pressures implied by ice stability modeling (*13, 53, 76*). Surficial water ice was not detected in Ceres' global regolith (*5*). However, it is conceivable that exposure of clays, hydrated salt and hydroxides to water vapor over geologic timescales may result in accumulation of adsorbed water within the regolith (*77*). Carbonaceous chondrites contain organic material with a molar H/C ratio of 0.7 (*19*). Analysis of a CI chondrite by (*18*) shows that organics contribute about 0.2 wt.% H, which implies the presence of a few weight percent organic matter.

The [Fe] in Ceres regolith (16 ± 1 wt.%) can be matched by adding 13 wt.% of a neutral component to the CI chondrite composition. The concentrations of both Fe and H can be explained if this neutral component were hydrogen-bearing organic matter. Thus, GRaND observations allow for the possibility that Ceres accreted materials with more organic matter than the CI parent body. If so, this would support the idea that the accreted materials or Ceres itself formed further away from the Sun than the meteorites (*1*). Alternatively, the relatively low-density organic matter could have been concentrated at the surface during ice-rock fractionation.

While organics are not required to fit the global spectrum measured by Dawn's Visible to near InfraRed (VIR) spectrometer (*1*), their presence cannot be excluded (*20*). Carbonates were detected with a spectral mixing fraction of 5%. If the spectral mixing fraction is interpreted as a mineral volume fraction, then carbonates would contribute about 0.7 wt.% C to the regolith, which is higher than the [C] in carbonates in CM chondrites (*78*). Carbon-bearing species may have been graphitized by exposure to ultraviolet radiation (*79*). The analysis of the VIR global spectrum found 60- to 90% of a

neutral, darkening agent, which was modeled as magnetite. The total concentration of Fe measured by GRaND implies less than 6 vol.% of magnetite within Ceres regolith. Thus, graphitized carbon is a viable alternative to magnetite as a darkening agent.

Hydrous mineral species detected by VIR include ammoniated phyllosilicates and OH bearing species, consistent with widespread aqueous alteration of surface materials. These observations support the analysis and interpretation of GRaND data presented in this study; however, we note that the H content implied by VIR spectral mixing fractions (approximately 3 wt.% WEH) is much lower than the bulk, ice-free regolith as seen by GRaND. This may relate to differences in the composition of the optical and bulk regolith (e.g. *80*) and/or uncertainties in converting spectral mixing fractions to mineral abundances.

Estimates of exogenic pollution

Ceres' regolith may contain significant contamination from the infall of exogenic impactors. Consequently, the composition of the uppermost regolith as seen by Dawn may not be representative of crustal materials. Here, we estimate the [Fe] and [H] in Ceres' pristine, upper crust just following formation, 4.5 Ga ago, given values observed by GRaND and hypothetical scenarios for the delivery of exogenic materials.

We computed the total mass delivered to the surface over the lifetime of Ceres (4.5 Gyr) using a recent collisional model (*81*). Collisions are stochastic, and large impacts may dominate the mass delivered. As a result, the accreted mass typically ranges from 1×10^{19} kg to 6×10^{19} kg. Here, we conservatively adopted 1×10^{19} kg. Based on the median excavation depth of all the impacts, the upper 5 km crustal layer contains the accreted material. Projectile retention efficiencies depend on the properties of the impactor and crust (*82*). Since the portion of accreted material retained in the crust is unknown, we estimated the pristine crustal composition for different retention efficiencies (from 0% to 50% in steps of 10%). The pristine composition was calculated for two end-member scenarios: accretion of S-type impactors modeled as representative ordinary chondrite composition (24 wt.% Fe and no H); and C-type impactors with representative CI/CM compositional average from Table S3 (20 wt.% Fe, 11 wt.% WEH) (*23*). We find that Ceres' pristine crust must have been richer in H and poorer in Fe than observed by GRaND (see Table S4).

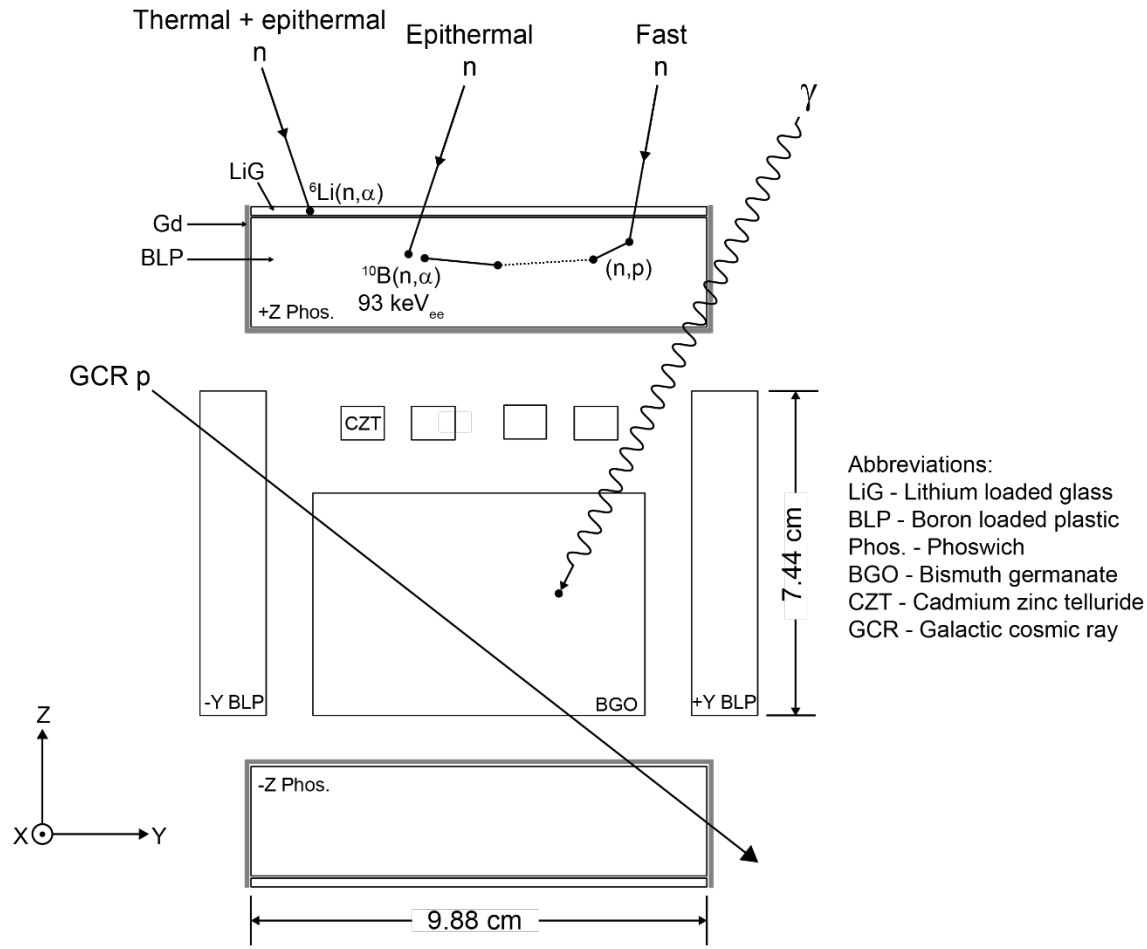

Fig. S1.
Cross section (Y-Z) showing the arrangement of sensors to scale within the GRaND instrument. GCR, neutron and gamma ray signatures are illustrated. The +Z axis points towards the center of Ceres during science data acquisition. See text for a description of GRaND sensors and data products.

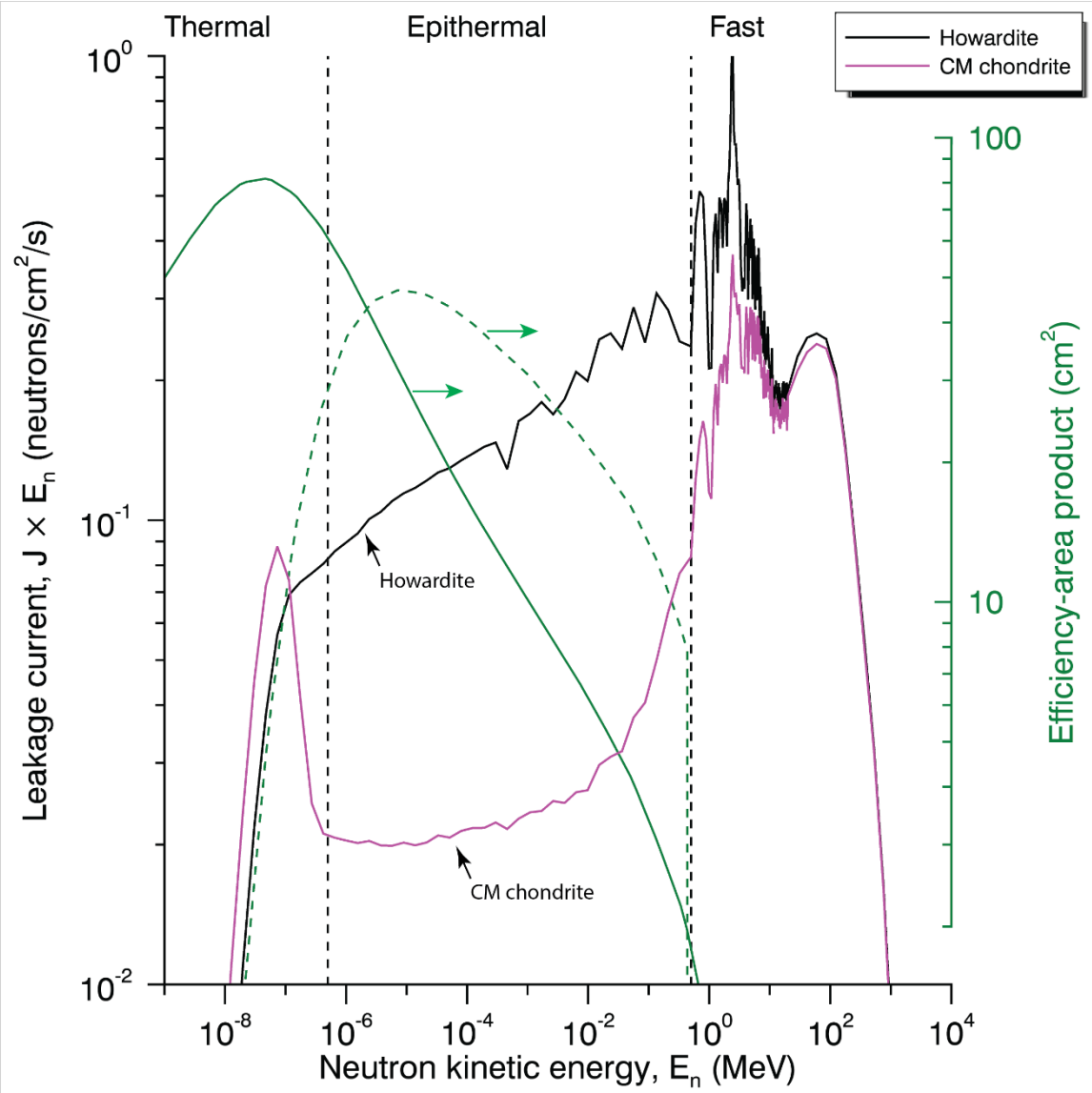

Fig. S2.
Neutron leakage spectra for howardite and CM chondrite compositions (left axis, legend) are compared. Efficiency-area products for the detection of thermal + epithermal (solid green) and epithermal neutrons (dashed green) are shown (right axis) (*9*). Approximate boundaries for neutron energy ranges are indicated (dashed vertical).

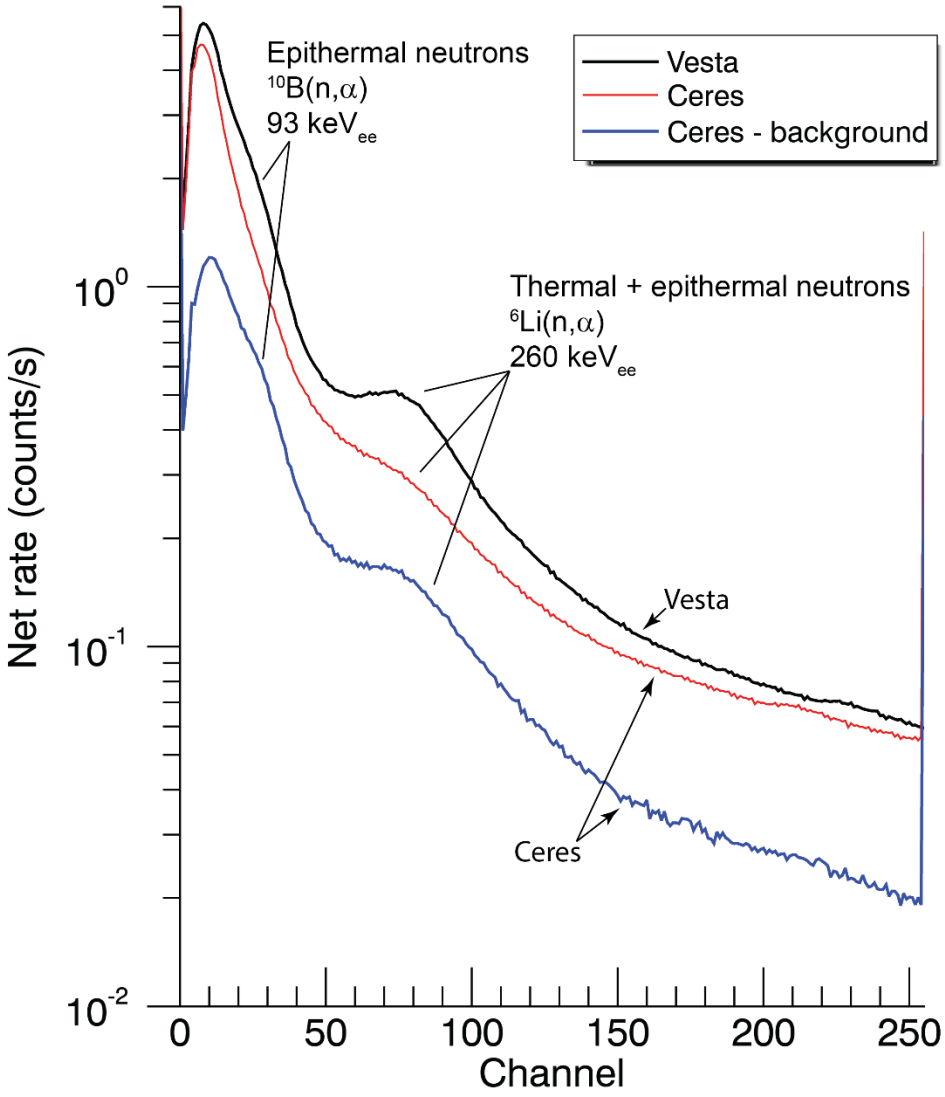

Fig. S3.
Spectra acquired by the +Z phoswich in LAMO at Vesta and Ceres. At Ceres, the 93 keV$_{ee}$ peak was not noticeable until background was subtracted. The spectrum labeled "Ceres – background" was formed by subtracting a fraction (0.9) of the background spectrum acquired far from Ceres from the spectrum measured in LAMO.

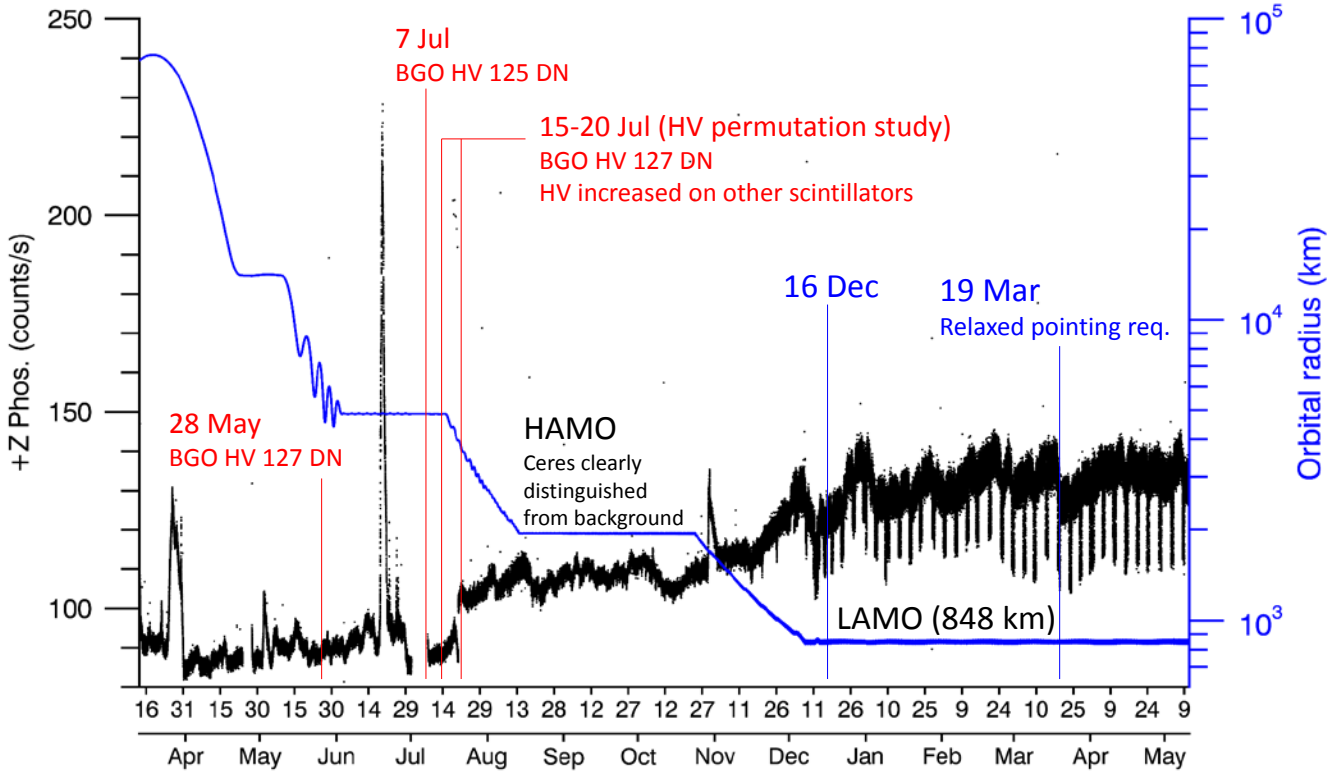

Fig. S4.
Timeline for GRaND data acquisition during Ceres encounter (2015-2016). Orbital radius and +Z phoswich gross counts are shown. Adjustments to instrument settings, including the high voltage (HV) applied to the BGO photomultiplier tube are marked (red). Settings are reported as data numbers (DN). From 16-Dec to 19-Mar, GRaND was pointed within 5° of nadir during science data acquisition. After 19-Mar, higher angles were allowed (up to about 10°), with negligible impact on mapped data.

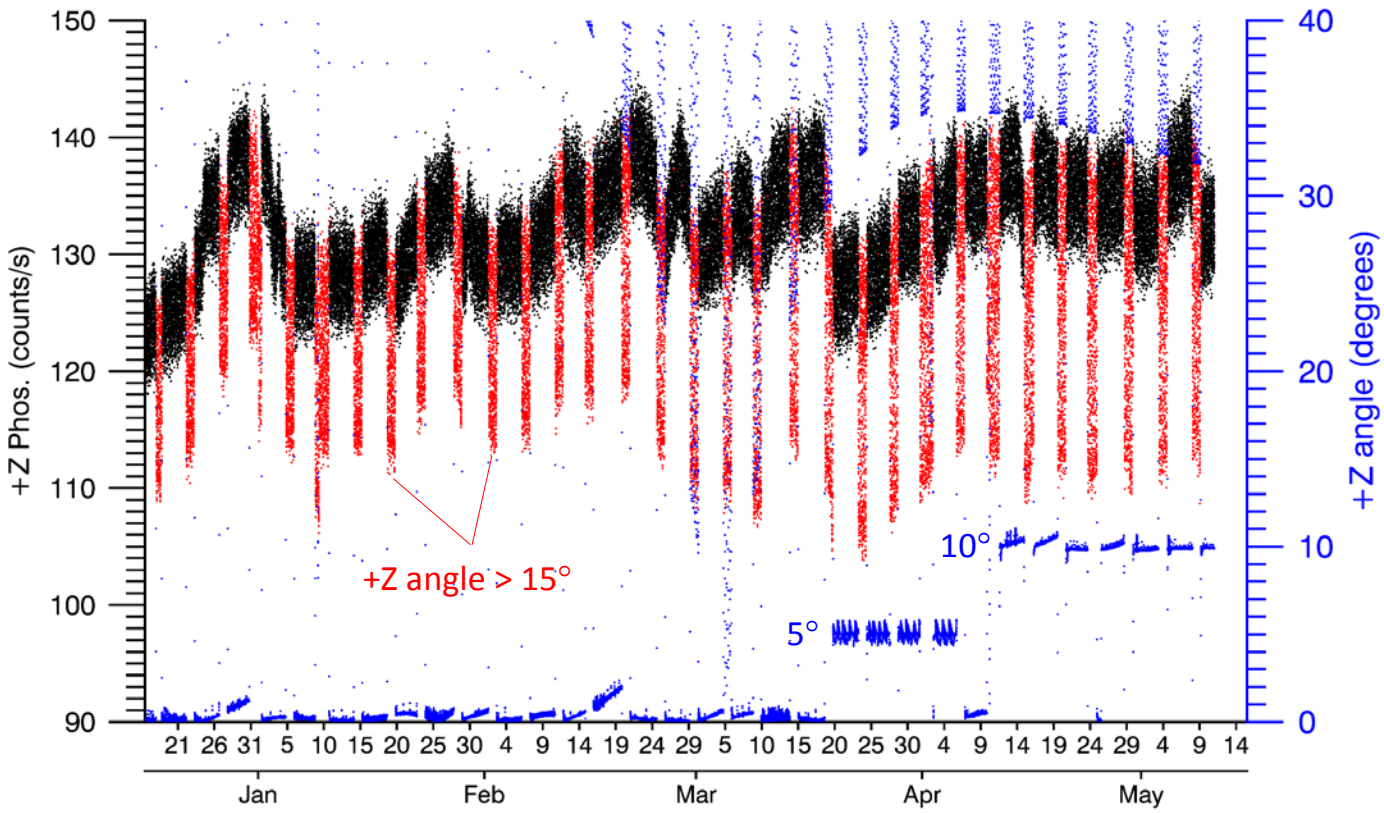

Fig. S5.
Pointing summary: Time series counting data acquired in LAMO for the +Z phoswich (left) and angle of the +Z axis relative to body center (right). The counting data are marked in red when the pointing angle exceeds 15°. When the instrument is tipped off center, the counting rate decreases, due to reduced counting efficiency (projected area) and shielding by spacecraft materials. Prior to 19-Mar, pointing angles greater than 5° were excluded from mapping/analysis. After 19-Mar, the exclusion angle was increased to 12°.

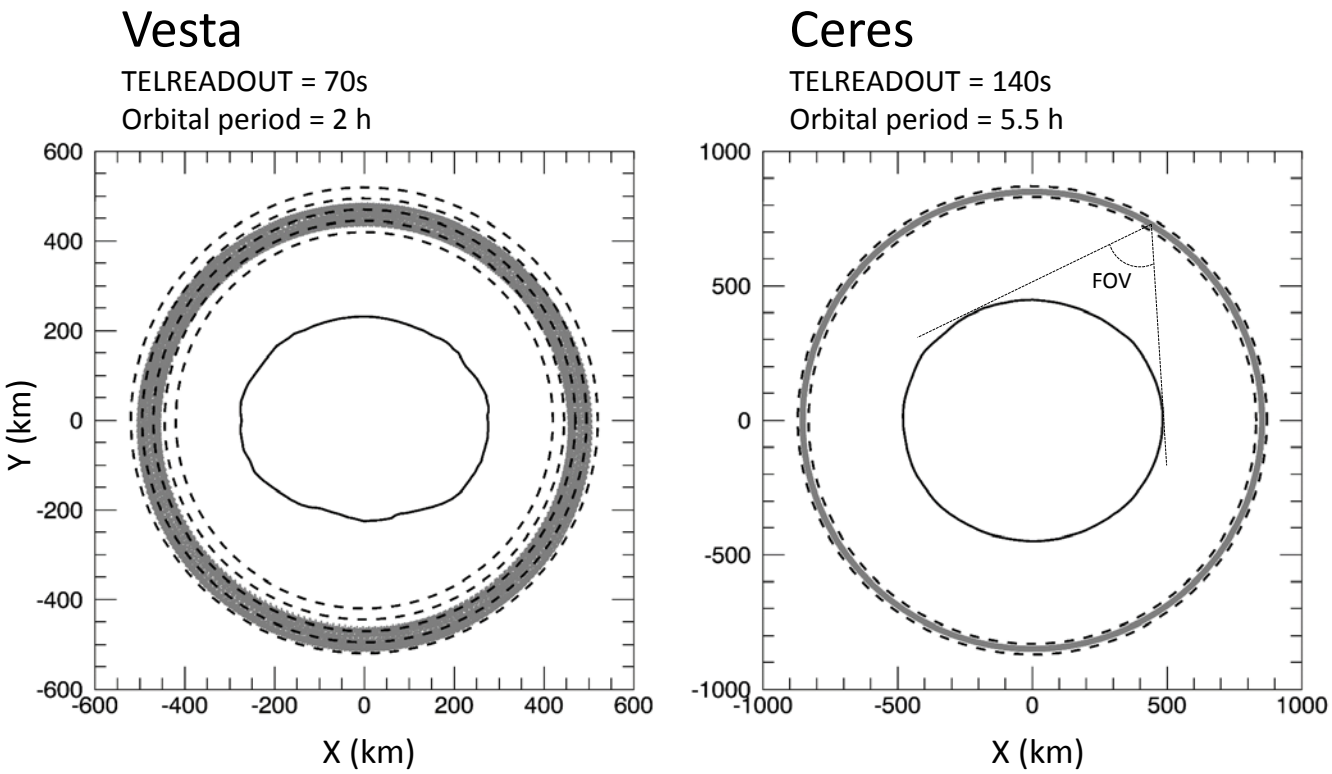

Fig. S6.
Orbital trajectories for the Dawn spacecraft at Vesta and Ceres are compared (grey lines). Circles (dashes) are plotted to show radial variations. The orbits were rotated onto a plane for display. Representative outlines for Vesta and Ceres are shown. GRaND's field of view (FOV) is illustrated for Ceres. The orbital period and science accumulation interval (TELREADOUT) are indicated.

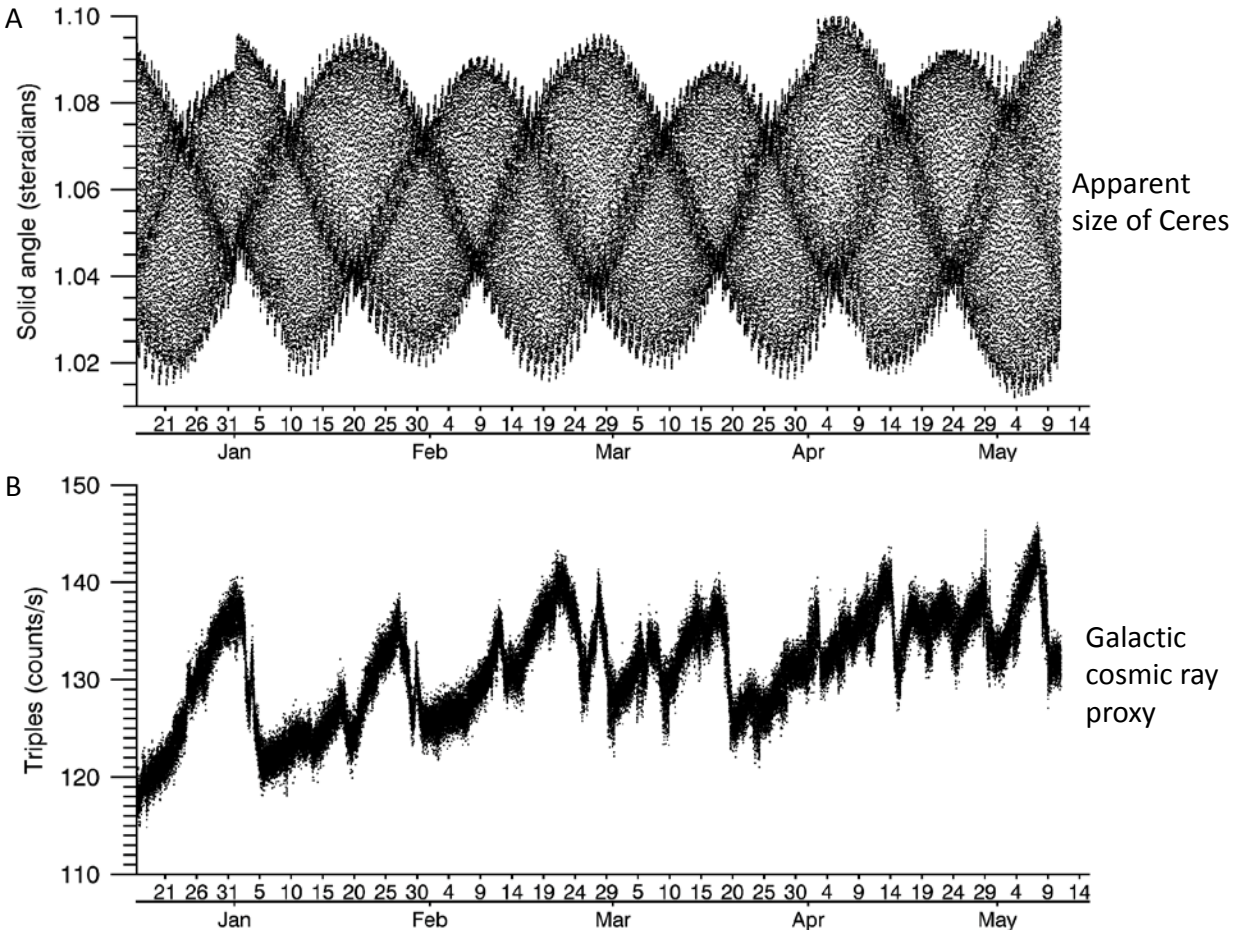

Fig. S7.
Measurement geometry and galactic cosmic ray proxy. (**A**) The apparent size of Ceres (solid angle); and (**B**) triples coincidence rate (proxy for the GCR flux) as a function of time in LAMO.

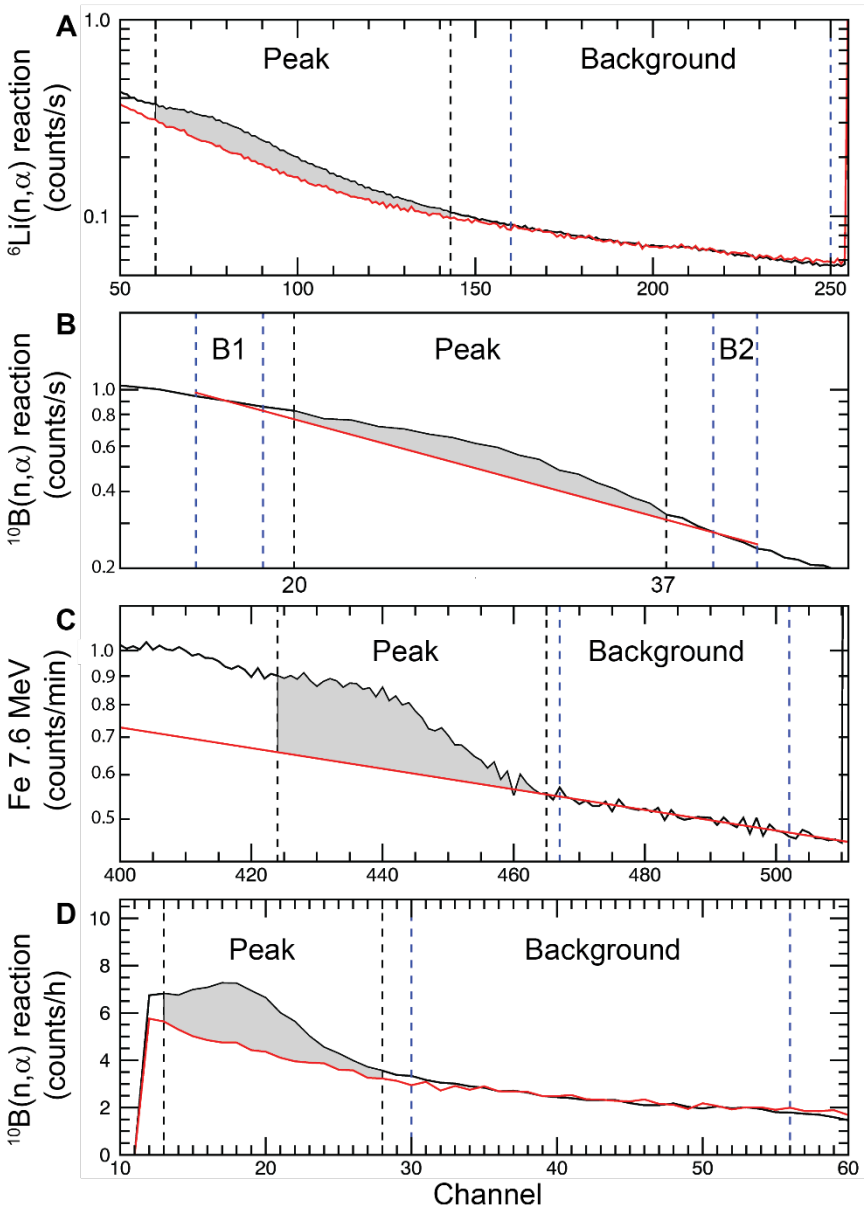

Fig. S8.
Peak extraction methods are illustrated using sums of LAMO pulse height spectra that meet pointing criteria. The net peak area is determined by subtracting background from gross counts within a region of interest (ROI) containing the peak (black dashed lines). The background shape function (red) is adjusted to match the spectrum within one or more background ROIs (blue dashed lines). The following spectra are shown: (**A**) +Z phoswich single interaction ^{6}Li(n,α) reaction peak; (**B**) +Z phoswich single interaction ^{10}B(n,α) reaction peak with background regions labeled B1 and B2; (**C**) BGO 7.6 MeV ^{56}Fe(n,γ) capture peak; (**D**) +Z phoswich double-pulse ^{10}B(n,α) second interaction peak. For the spectrum shown in (**B**), the background measured far from Ceres was scaled and subtracted from the single interaction spectra acquired in LAMO (as in Fig. S3).

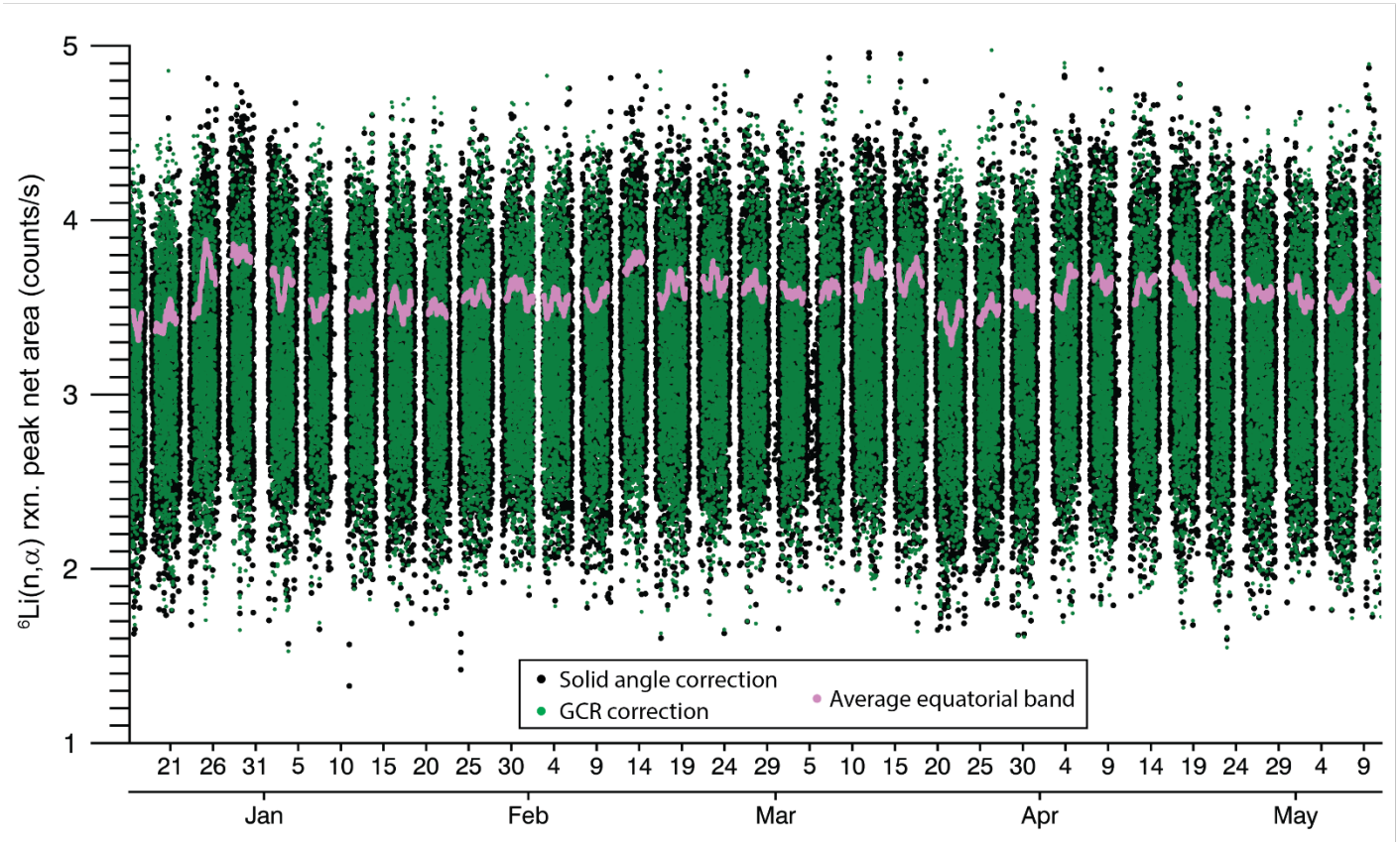

Fig. S9.

Galactic cosmic ray corrections. ^{6}Li(n,α) net peak areas corrected for solid angle variations (black points) were further corrected for GCR variations (green points). The GCR correction factor varies inversely with the average counting rate in an equatorial band (30°S to 30°N) within a 3.5 orbit window (violet points).

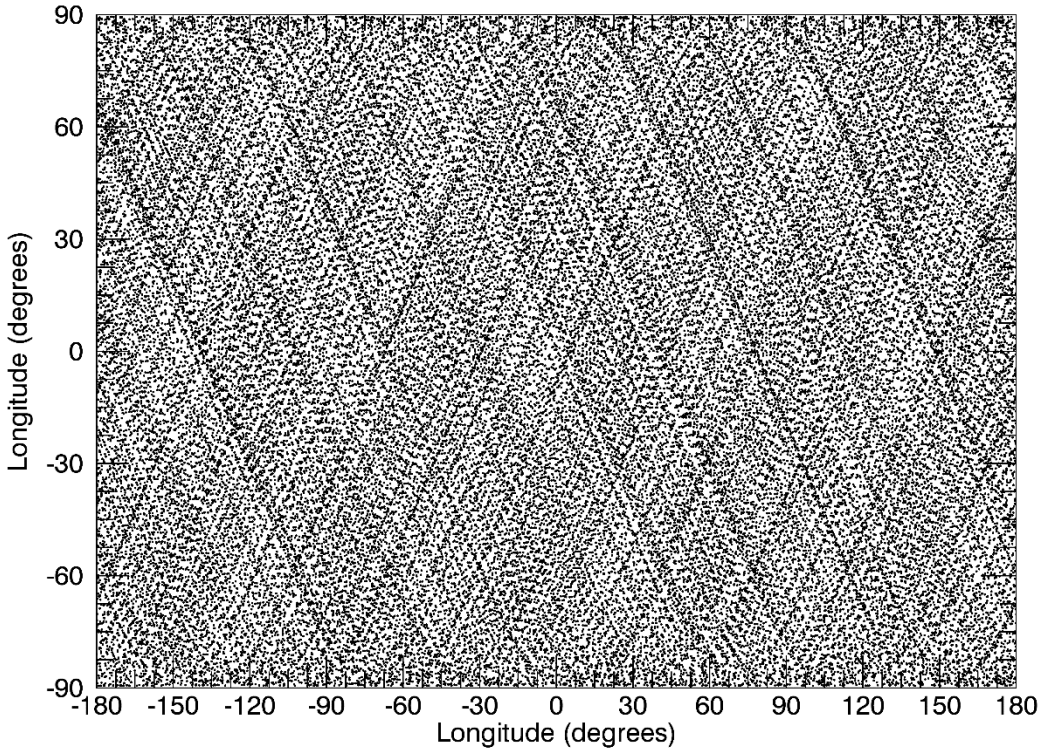

Fig. S10.
Dawn's orbit provided full, global coverage of Ceres. The chart shows the distribution of sub-satellite points sampled by Dawn's circular polar, low altitude mapping orbit at Ceres.

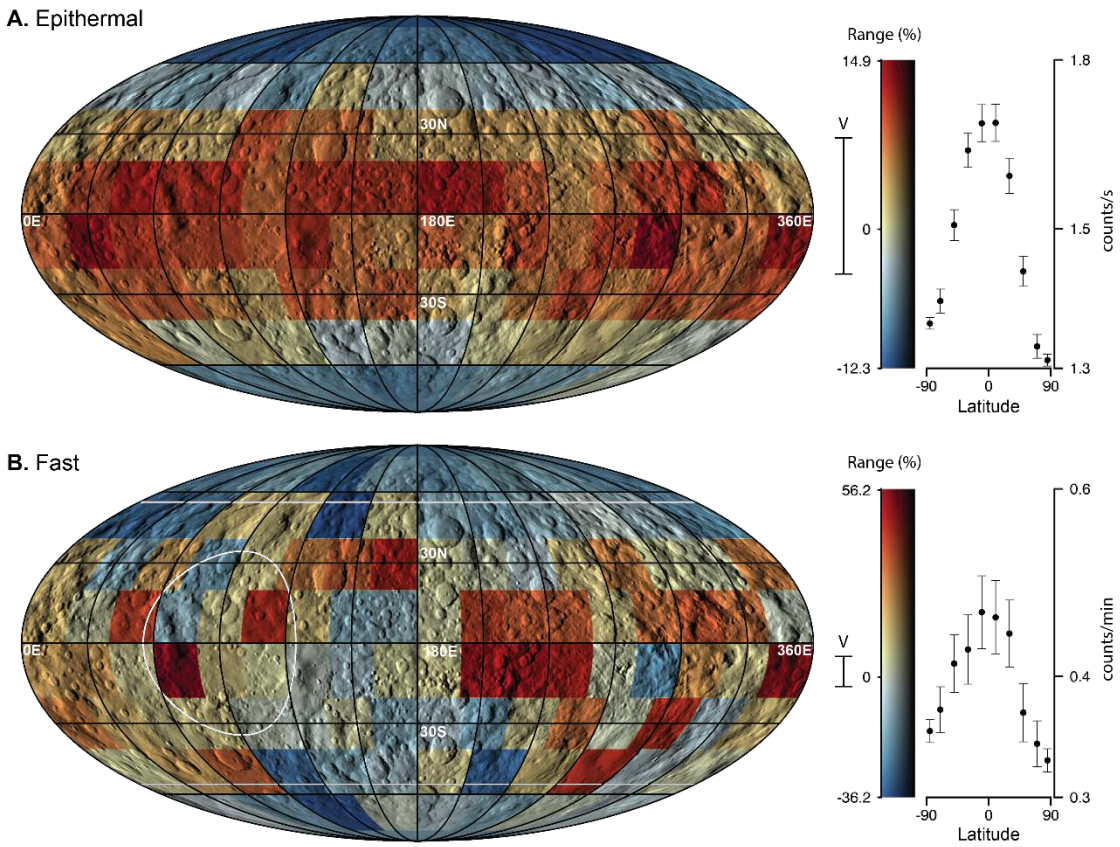

Fig. S11.
Maps of corrected counting rates for epithermal and fast neutrons. See Fig. 1 for a description of map annotations and scale.

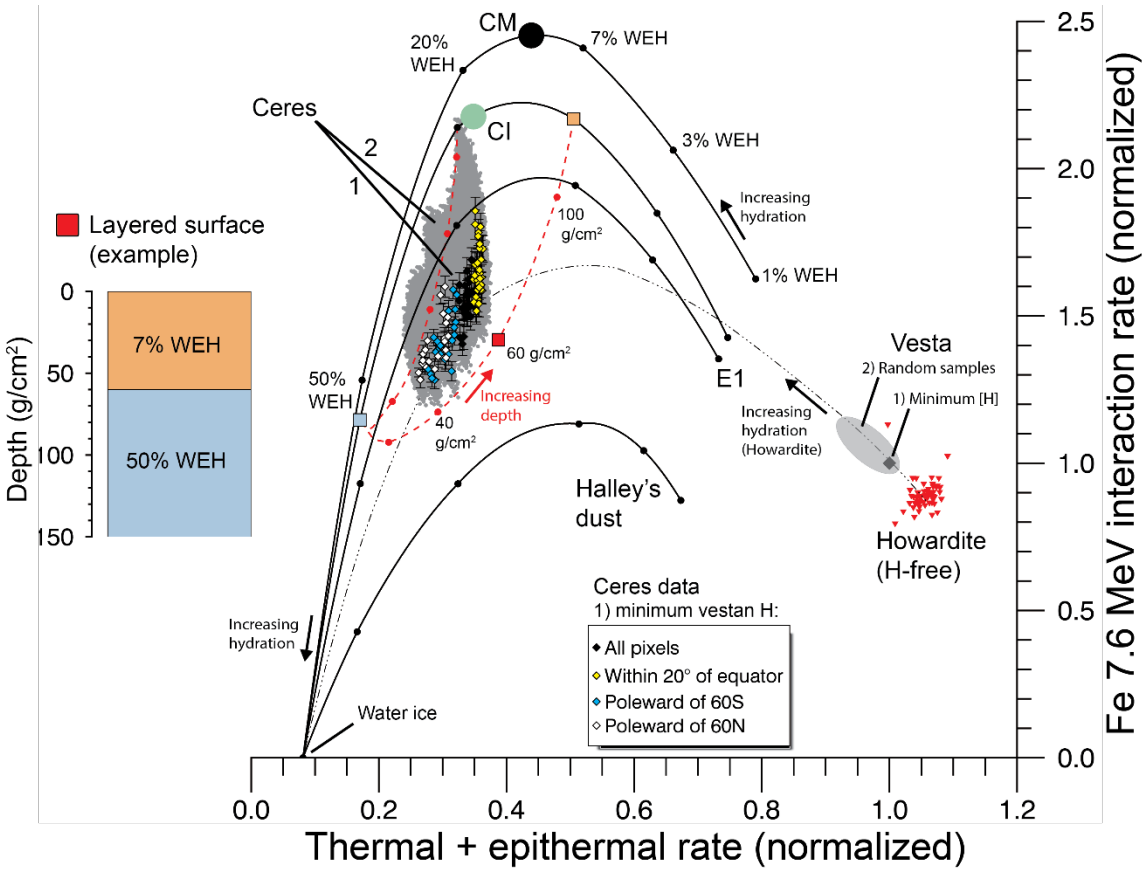

Fig. S12.
Sensitivity of neutron and gamma ray counting rates to analysis assumptions. Figure 2 is repeated to show the sensitivity of the placement of map data on a relative scale with models to assumptions regarding the average composition of Vesta's regolith. Two cases are shown: 1) minimum [H] with H-free howardite composition containing 55% eucrite (see legend); 2) random samples of Vesta's global regolith for a selected range of howardite compositions mixed with H (grey points and oval). Increasing the [H] of Vesta's regolith shift's Vesta's counting rates along the line of hydration for howardite, which in turn pushes the cerean data cloud towards the hydration line for CI chondrites. The individual points labeled "CI" and "CM" correspond to the CI- and CI-chondrite compositions given in Table S1.

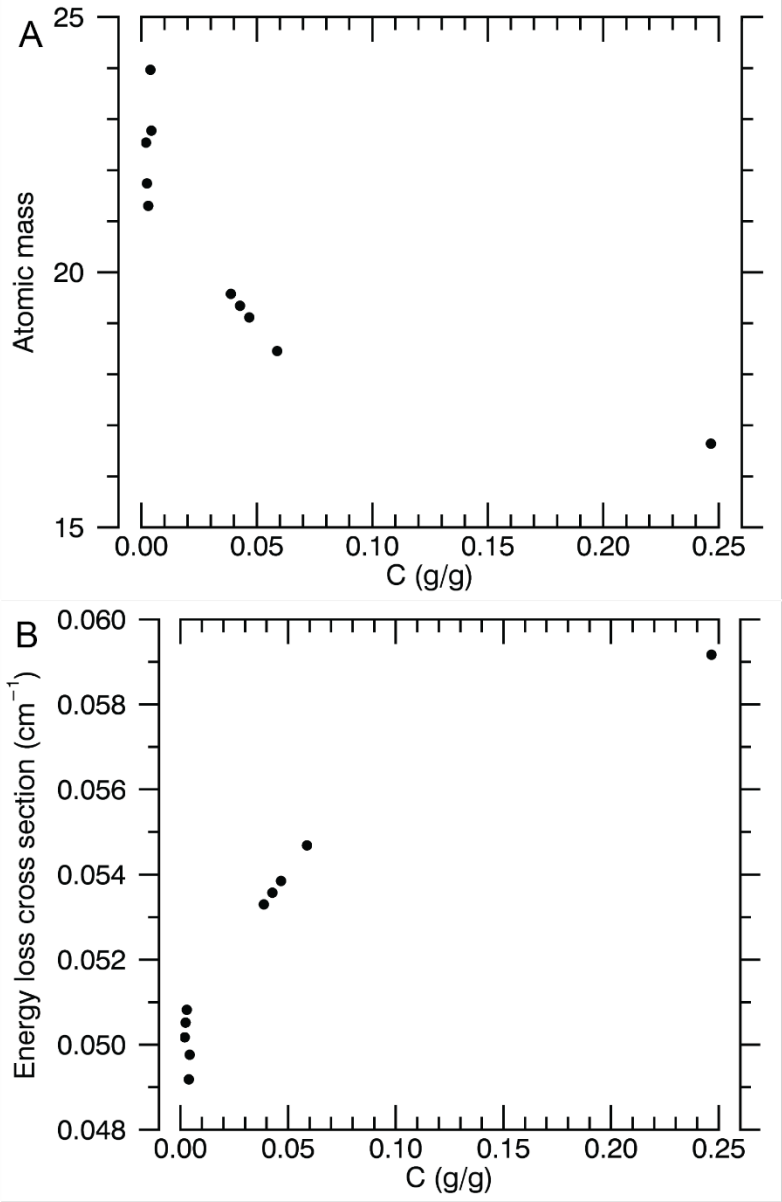

Fig. S13.
Neutron macroparameters for model regolith materials as a function of C content: (**A**) the number density weighted average atomic mass; (**B**) the macroscopic energy loss cross section. Fast neutron production varies with average atomic mass, and the flux of epithermal neutrons varies inversely with the energy loss cross section (*9*). For further details on the theory of neutron moderation see (*62*, *83*).

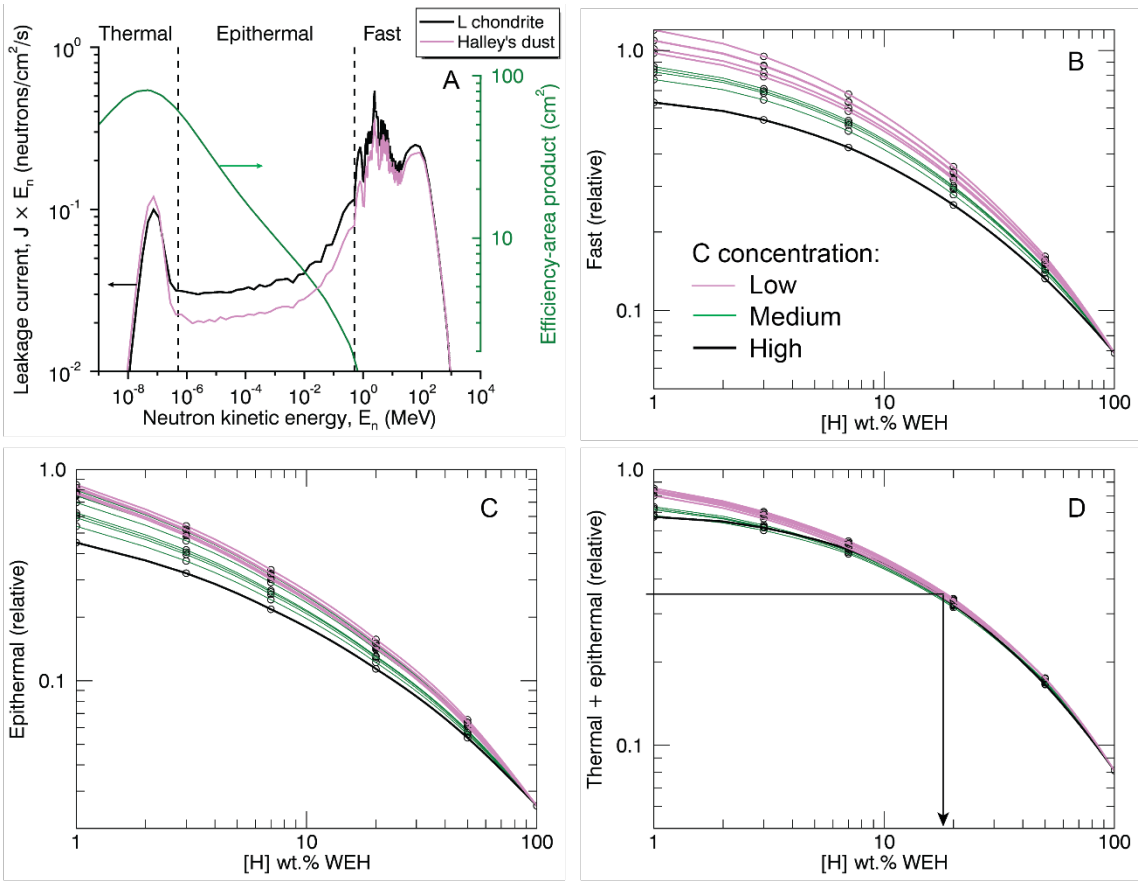

Fig. S14.

Variation of neutron counting rates with C and H content: (**A**) For materials with the same [H] (7 wt.% WEH illustrated), materials with higher C content (Halley's dust here) have lower epithermal and higher thermal leakage currents. (**B-D**) Relative counting rates for fast, epithermal, and thermal + epithermal neutrons as a function of [H] for model materials with low (ordinary chondrite), medium (extrapolated carbonaceous compositions, Table S1), and high (Halley's dust) concentrations of C. Trends for thermal + epithermal counts do not depend strongly on C concentration when [H] is greater than 10 wt.% WEH. Consequently, the thermal + epithermal measurements can be used independently to determine [H] (e.g., lines terminating with black arrow).

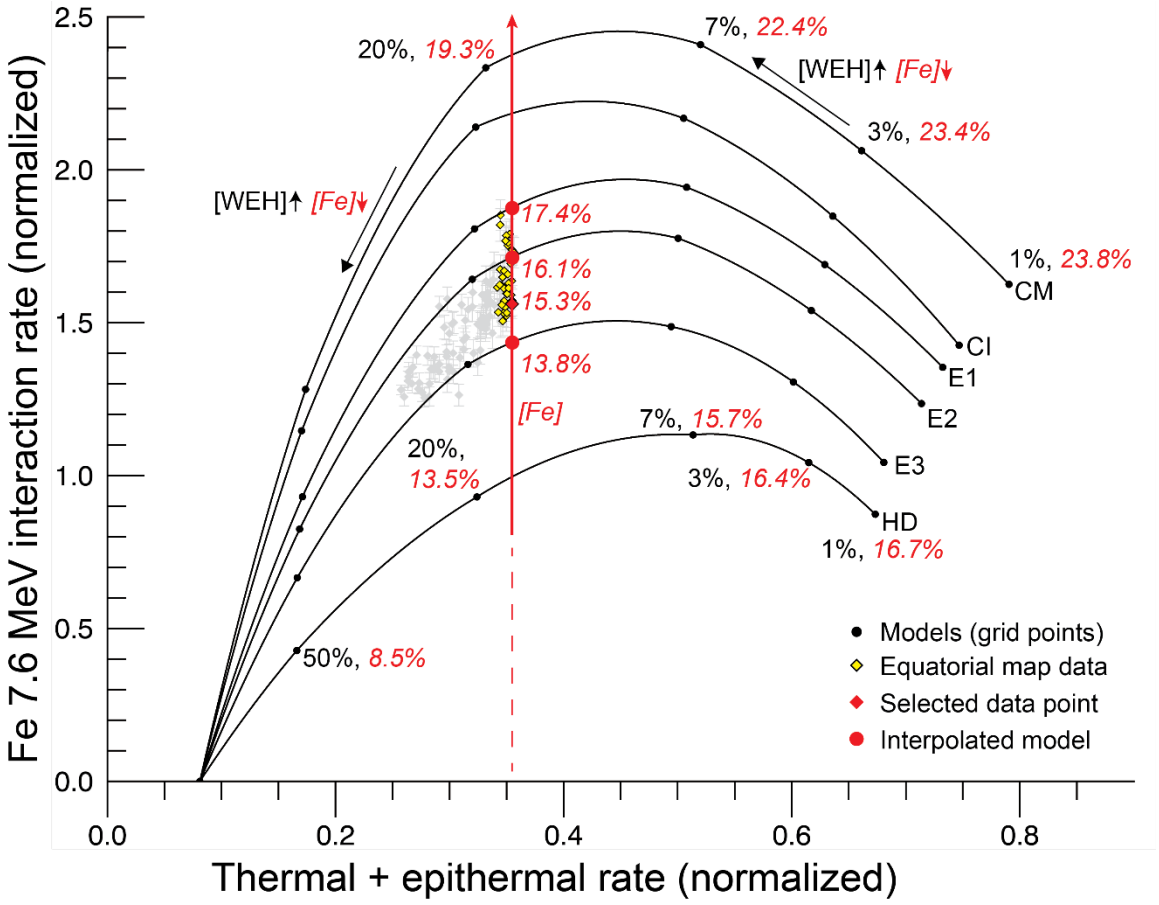

Fig. S15.

Determination of Fe concentration. The model hydration trends form an interpolation grid that can be used to determine [Fe] for equatorial pixels (within 20° of the equator). For each model composition, the concentration of Fe (wt.%, red italics) decreases with added [H] (wt.% WEH, black text), e.g. trends for CM chondrite and Halley's dust (HD) are labeled. For constant thermal + epithermal rate (constant [H]), the concentration of [Fe] varies with the Fe 7.6 MeV interaction rate. The interpolation process is illustrated for a selected equatorial data point (red diamond). A vertical line, corresponding to the measured thermal + epithermal rate, transects the grid. For model composition, the [Fe] and Fe 7.6 MeV rate is determined at the intersection point (e.g., red circles). The [Fe] for the pixel is determined by linear interpolation, given the measured Fe 7.6 MeV rate.

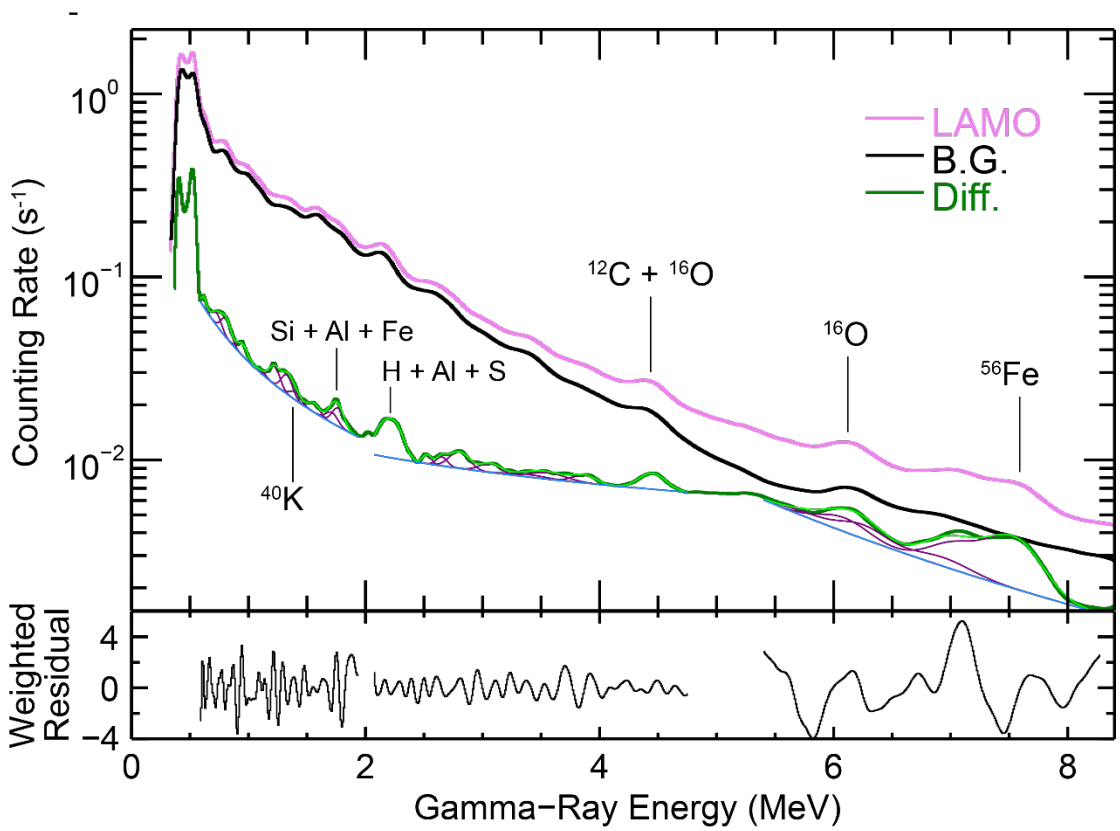

Fig. S16.
Difference spectrum is sensitive to the composition of Ceres. Peak areas for selected reactions were extracted from a difference spectrum (green), formed by subtracting a background spectrum measured far from Ceres (black) from spectra acquired in LAMO (violet). The background spectrum was corrected for changes in the GCR flux between the background and LAMO accumulation periods. Fitted power-law backgrounds (light blue), Gaussian full-energy peaks (purple), and total fits (light green) are shown along with weighted residuals.

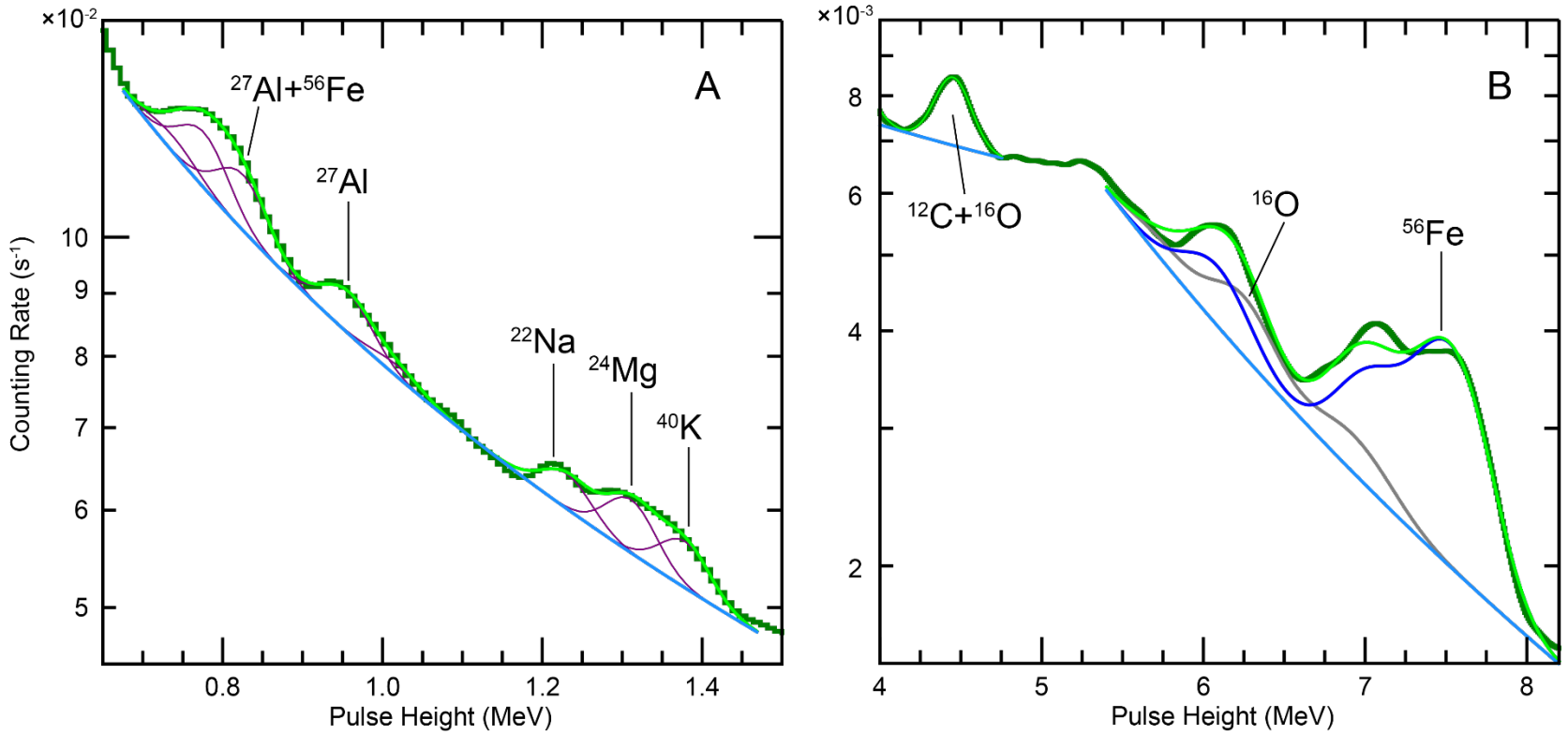

Fig. S17.
Regional peak analyses of difference spectra: (**A**) Low energy region containing the 1.4 MeV gamma ray from the decay of ^{40}K (difference spectrum); (**B**) high energy region containing contributions from neutron nonelastic scattering with ^{12}C and ^{16}O (4.4 MeV), inelastic scattering with ^{16}O (6.1 MeV), and radiative neutron capture with ^{56}Fe (7.6 MeV) (GCR-weighted difference spectrum, Fig. S16). Fitted power law backgrounds (light blue), Gaussian full energy peaks (purple), and total fits (light green) are shown. In panel (**B**), O and Fe contributions are grey and blue, respectively.

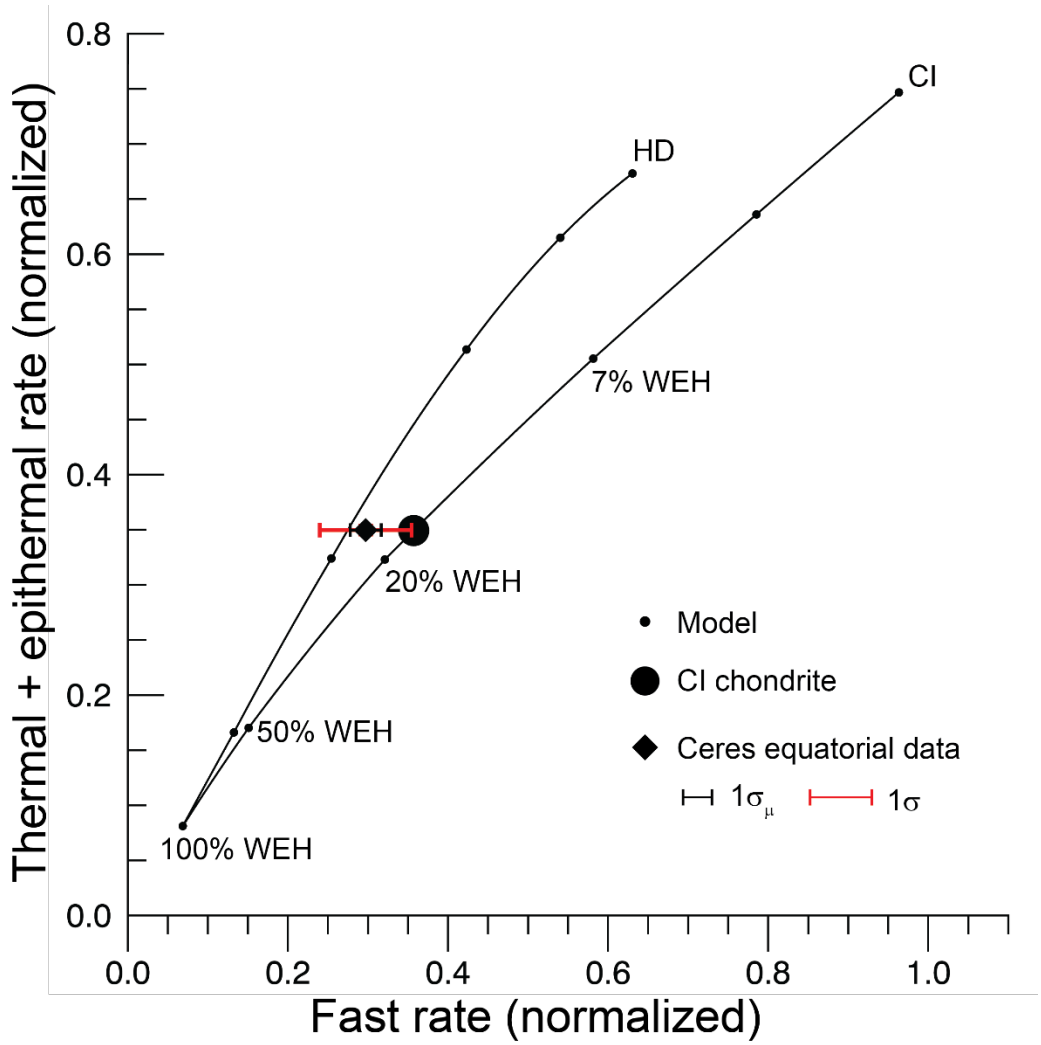

Fig. S18.
Comparison of normalized neutron counting rates with models. Ceres' equatorial mean counting rates (pixels within 20° of the equator) are compared with models, including hydration trends for CI chondrite and Halley's dust (HD). The uncertainty in the mean ($1\sigma_\mu$) and spread of the data (population standard deviation, 1σ) is shown. The error bars are smaller than the symbol for thermal + epithermal rates. Selected model values are labeled with H concentration (wt.% WEH). The minimum hydrogen content for Vesta's regolith was assumed. The normalized fast rate is insensitive to assumptions regarding Vesta's composition.

Table S1.

Model compositions used in the analysis of GRaND data. Materials include CM and CI chondrite averages (*23*), extrapolated compositions E1-3, and Halley's dust (HD) (*47*).

Z	Symbol	Units	CM	CI	E1	E2	E3	HD
	WEH	wt. %	12.6	18.1	20.2	21.9	28.9	45.1
1	H	wt.%	1.40	2.02	2.24	2.44	3.22	5.01
3	Li	$\mu g\ g^{-1}$	1.50	1.50	1.50	1.49	1.49	
5	B	$\mu g\ g^{-1}$	0.48	0.87	1.01	1.13	1.63	
6	C	wt.%	2.20	3.44	3.90	4.30	5.87	24.15
7	N	$mg\ g^{-1}$	1.52	3.17	3.79	4.31	6.40	14.54
8	O	wt.%	43.3	46.3	47.5	48.4	52.3	35.2
11	Na	$mg\ g^{-1}$	3.91	4.99	5.39	5.74	7.11	5.69
12	Mg	wt.%	11.5	9.7	9.0	8.4	6.1	5.9
13	Al	wt.%	1.1	0.9	0.8	0.7	0.3	0.5
14	Si	wt.%	12.7	10.6	9.8	9.1	6.4	12.8
16	S	wt.%	2.70	5.40	6.40	7.25	10.66	5.70
17	Cl	$\mu g\ g^{-1}$	431	699	798	883	1222	
19	K	$\mu g\ g^{-1}$	371	549	615	672	897	193
20	Ca	wt.%	1.29	0.92	0.79	0.67	0.21	0.62
22	Ti	$\mu g\ g^{-1}$	551	439	398	363	222	475
24	Cr	$mg\ g^{-1}$	3.05	2.65	2.49	2.36	1.85	1.16
25	Mn	$mg\ g^{-1}$	1652	1937	2042	2132	2492	680
26	Fe	wt.%	21.3	18.2	17.0	16.0	12.0	7.2
27	Co	$\mu g\ g^{-1}$	561	504	483	465	394	438
28	Ni	wt.%	1.23	1.10	1.05	1.01	0.84	0.60
62	Sm	$ng\ g^{-1}$	204.3	149.7	129.6	112.3	43.3	
63	Eu	$ng\ g^{-1}$	78.1	56.9	49.1	42.4	15.5	
64	Gd	$ng\ g^{-1}$	290.4	199.7	166.1	137.4	22.6	
90	Th	$ng\ g^{-1}$	41.1	30.8	27.1	23.8	10.9	

Table S2.

Gamma-ray peak areas for Vesta and Ceres. Counting rates for gamma rays observed within a ±20° equatorial latitude band at Ceres are compared with global averages for Vesta. Carbon, O, and Fe net peak areas (counts/s) were extracted from the GCR-corrected difference spectrum; whereas, the K peak area was determined from a spectrum formed by simple difference (LAMO – background). The contribution of gamma rays induced by nonelastic scattering with O to the 4.4 MeV peak was estimated from the area of the 6.1 MeV O-inelastic peak, given flux-weighted gamma ray production rates, and the relative efficiency of the detector. This contribution was subtracted to determine the contribution of C to the 4.4 MeV peak.

		Ceres		Vesta	
Energy (MeV)	Primary Source	Rate (cps)*	uncertainty (1σ)	Rate (cps)	uncertainty (1σ)
7.6	**Fe**	0.121	3%	0.067	1%
6.1	**O**	0.036	5%	0.080	1%
4.4	**C+O**	0.049	7%	0.053	2%
	C	0.032	13%	0.014	7%
1.4	**K**	0.045	9%	0.064	2%

*Counts per second.

Table S3.

Water equivalent hydrogen (WEH) and Fe contents of selected meteorites. Water equivalent hydrogen concentrations were determined from mass spectrometry (mass spec.) (*18*) (WEH = 9 × [H]) and thermogravimetric analyses (TGA) (*72*). Except where noted, TGA analyses are based on mass loss between 400- and 770-°C. Refrences for Fe analyses are listed. In four cases, Fe values were assigned based on pairing groups (with meteorite ALH 83100) (*18*).

		Water equivalent hydrogen				
Meteorite	Class.	Mass spec. (wt.%)	TGA (wt.%)	Fe (wt.%)	Ref.	Pairing
Orgueil	CI	14.0	17.4	18.5	(*84*)	
Ivuna	CI	13.7	18.9	18.6	(*84*)	
ALH 83100	CM	13.1	13.9	20.3	(*85*)	
ALH 84029	CM	12.2	13.3	20.3	(*85*)	ALH 83100
ALH 84044	CM	12.0	12.9	20.3	(*85*)	ALH 83100
MET 01070	CM	12.3	11.1	22.9	(*86*)	
QUE 97990	CM	9.4	8.7	19.2	(*86*)	
Murchison	CM	9.6	10.8	20.5	(*86*)	
Cold Bokkeveld	CM2	12.2		19.8	(*86*)	
Murray	CM2	10.4		21.3	(*86*)	
Nagoya	CM2	12.7		20.2	(*86*)	
Nogoya*	CM2	10.0		20.2	(*86*)	
Banten	CM2	9.2		21.1	(*87*)	
Essebi	C2 ungrouped	8.4		20.2	(*88*)	
Mighei	CM2	10.2		21.3	(*89*)	
ALH 84034	CM2	12.6		20.3	(*85*)	ALH 83100
ALH 84042	CM2	12.1		20.3	(*85*)	ALH 83100

*For H analysis, sample crushed under acetone (*18*).

Table S4.

Effect of exogenic contamination. Estimates of the composition of Ceres' "pristine" upper crust, prior to the infall of S-type or C-type impactors, as a function of projectile retention efficiency. The "exogenic portion" is the percentage by mass of exogenic material contained in Ceres' present-day crust. Because Ceres' composition is similar to that of the carbonaceous chondrites, for C-type impactors the change in pristine composition from that measured by GRaND is smaller than for S-type impactors. The composition of the impactors and retention efficiencies are unknown.

		Pristine crustal composition			
		S-type impactors		C-type impactors	
Retention efficiency (%)	Exogenic portion (%)	[H] (wt.%)	[Fe] (wt.%)	[H] (wt.%)	[Fe] (wt.%)
0	0	17.0	16.0	17.0	16.0
10	5	17.9	15.6	17.3	15.8
20	10	18.8	15.2	17.6	15.5
30	14	19.9	14.7	17.9	15.3
40	19	21.0	14.1	18.3	15.0
50	24	22.4	13.5	18.8	14.6

References and Notes

1. M. C. De Sanctis, E. Ammannito, A. Raponi, S. Marchi, T. B. McCord, H. Y. McSween, F. Capaccioni, M. T. Capria, F. G. Carrozzo, M. Ciarniello, A. Longobardo, F. Tosi, S. Fonte, M. Formisano, A. Frigeri, M. Giardino, G. Magni, E. Palomba, D. Turrini, F. Zambon, J.-P. Combe, W. Feldman, R. Jaumann, L. A. McFadden, C. M. Pieters, T. Prettyman, M. Toplis, C. A. Raymond, C. T. Russell, Ammoniated phyllosilicates with a likely outer solar system origin on (1) Ceres. *Nature* **528**, 241–244 (2015). doi:10.1038/nature16172 Medline

2. T. B. McCord, C. Sotin, Ceres: Evolution and current state. *J. Geophys. Res.* **110**, E05009 (2005). doi:10.1029/2004JE002244

3. J. C. Castillo-Rogez, T. B. McCord, Ceres' evolution and present state constrained by shape data. *Icarus* **205**, 443–459 (2010). doi:10.1016/j.icarus.2009.04.008

4. M. Neveu, S. J. Desch, Geochemistry, thermal evolution, and cryovolcanism on Ceres with a muddy ice mantle. *Geophys. Res. Lett.* **42**, 10197–10206 (2015). doi:10.1002/2015GL066375

5. J. P. Combe, T. B. McCord, F. Tosi, E. Ammannito, F. G. Carrozzo, M. C. De Sanctis, A. Raponi, S. Byrne, M. E. Landis, K. H. G. Hughson, C. A. Raymond, C. T. Russell, Detection of local H_2O exposed at the surface of Ceres. *Science* **353**, aaf3010 (2016). doi:10.1126/science.aaf3010 Medline

6. F. P. Fanale, J. R. Salvail, The water regime of asteroid (1) Ceres. *Icarus* **82**, 97–110 (1989). doi:10.1016/0019-1035(89)90026-2

7. R. S. Park, A. S. Konopliv, B. G. Bills, N. Rambaux, J. C. Castillo-Rogez, C. A. Raymond, A. T. Vaughan, A. I. Ermakov, M. T. Zuber, R. R. Fu, M. J. Toplis, C. T. Russell, A. Nathues, F. Preusker, A partially differentiated interior for (1) Ceres deduced from its gravity field and shape. *Nature* **537**, 515–517 (2016). doi:10.1038/nature18955 Medline

8. P. A. Bland, M. D. Jackson, R. F. Coker, B. A. Cohen, J. B. W. Webber, M. R. Lee, C. M. Duffy, R. J. Chater, M. G. Ardakani, D. S. McPhail, D. W. McComb, G. K. Benedix, Why aqueous alteration in asteroids was isochemical: High porosity ≠ high permeability. *Earth Planet. Sci. Lett.* **287**, 559–568 (2009). doi:10.1016/j.epsl.2009.09.004

9. T. H. Prettyman, W. C. Feldman, H. Y. McSween, R. D. Dingler, D. C. Enemark, D. E. Patrick, S. A. Storms, J. S. Hendricks, J. P. Morgenthaler, K. M. Pitman, R. C. Reedy, Dawn's gamma ray and neutron detector. *Space Sci. Rev.* **163**, 371–459 (2011). doi:10.1007/s11214-011-9862-0

10. See supplementary materials.

11. T. H. Prettyman, D. W. Mittlefehldt, N. Yamashita, D. J. Lawrence, A. W. Beck, W. C. Feldman, T. J. McCoy, H. Y. McSween, M. J. Toplis, T. N. Titus, P. Tricarico, R. C. Reedy, J. S. Hendricks, O. Forni, L. Le Corre, J.-Y. Li, H. Mizzon, V. Reddy, C. A. Raymond, C. T. Russell, Elemental mapping by Dawn reveals exogenic H in Vesta's regolith. *Science* **338**, 242–246 (2012). doi:10.1126/science.1225354 Medline

12. E. Ammannito, M. C. DeSanctis, M. Ciarniello, A. Frigeri, F. G. Carrozzo, J.-P. Combe, B. L. Ehlmann, S. Marchi, H. Y. McSween, A. Raponi, M. J. Toplis, F. Tosi, J. C. Castillo-

Rogez, F. Capaccioni, M. T. Capria, S. Fonte, M. Giardino, R. Jaumann, A. Longobardo, S. P. Joy, G. Magni, T. B. McCord, L. A. McFadden, E. Palomba, C. M. Pieters, C. A. Polanskey, M. D. Rayman, C. A. Raymond, P. M. Schenk, F. Zambon, C. T. Russell, Distribution of phyllosilicates on the surface of Ceres. *Science* **353**, aaf4279 (2016). doi:10.1126/science.aaf4279 Medline

13. N. Schorghofer, Predictions of depth-to-ice on asteroids based on an asynchronous model of temperature, impact stirring, and ice loss. *Icarus* **276**, 88–95 (2016). doi:10.1016/j.icarus.2016.04.037

14. W. C. Feldman *et al*., Global distribution of near-surface hydrogen on Mars. *J. Geophys. Res.* **109**, E09006 (2004). doi:10.1029/2003JE002160

15. D. T. Britt, G. J. S. J. Consolmagno, Stony meteorite porosities and densities: A review of data through 2001. *Meteorit. Planet. Sci.* **38**, 1161–1180 (2003). doi:10.1111/j.1945-5100.2003.tb00305.x

16. M. Küppers, L. O'Rourke, D. Bockelée-Morvan, V. Zakharov, S. Lee, P. von Allmen, B. Carry, D. Teyssier, A. Marston, T. Müller, J. Crovisier, M. A. Barucci, R. Moreno, Localized sources of water vapour on the dwarf planet (1) Ceres. *Nature* **505**, 525–527 (2014). doi:10.1038/nature12918 Medline

17. C. T. Russell, C. A. Raymond, E. Ammannito, D. L. Buczkowski, M. C. De Sanctis, H. Hiesinger, R. Jaumann, A. S. Konopliv, H. Y. McSween, A. Nathues, R. S. Park, C. M. Pieters, T. H. Prettyman, T. B. McCord, L. A. McFadden, S. Mottola, M. T. Zuber, S. P. Joy, C. Polanskey, M. D. Rayman, J. C. Castillo-Rogez, P. J. Chi, J. P. Combe, A. Ermakov, R. R. Fu, M. Hoffmann, Y. D. Jia, S. D. King, D. J. Lawrence, J.-Y. Li, S. Marchi, F. Preusker, T. Roatsch, O. Ruesch, P. Schenk, M. N. Villarreal, N. Yamashita, Dawn arrives at Ceres: Exploration of a small, volatile-rich world. *Science* **353**, 1008–1010 (2016). doi:10.1126/science.aaf4219 Medline

18. C. M. O'D. Alexander, R. Bowden, M. L. Fogel, K. T. Howard, C. D. K. Herd, L. R. Nittler, The provenances of asteroids, and their contributions to the volatile inventories of the terrestrial planets. *Science* **337**, 721–723 (2012). doi:10.1126/science.1223474 Medline

19. S. Derenne, F. Robert, Model of molecular structure of the insoluble organic matter isolated from Murchison meteorite. *Meteorit. Planet. Sci.* **45**, 1461–1475 (2010). doi:10.1111/j.1945-5100.2010.01122.x

20. A. Garenne, P. Beck, G. Montes-Hernandez, O. Brissaud, B. Schmitt, E. Quirico, L. Bonal, C. Beck, K. T. Howard, Bidirectional reflectance spectroscopy of carbonaceous chondrites: Implications for water quantification and primary composition. *Icarus* **264**, 172–183 (2016). doi:10.1016/j.icarus.2015.09.005

21. E. D. Young, K. K. Zhang, G. Schubert, Conditions for pore water convection within carbonaceous chondrite parent bodies – implications for planetesimal size and heat production. *Earth Planet. Sci. Lett.* **213**, 249–259 (2003). doi:10.1016/S0012-821X(03)00345-5

22. A. J. Brearley, Nebular versus parent-body processing. *Treatise on Geochemistry* **1**, 711 (2003).

23. K. Lodders, B. Fegley Jr., *The Planetary Scientist's Companion* (Oxford University Press on Demand, 1998).

24. M. Humayun, R. N. Clayton, Potassium isotope cosmochemistry: Genetic implications of volatile element depletion. *Geochim. Cosmochim. Acta* **59**, 2131–2148 (1995). doi:10.1016/0016-7037(95)00132-8

25. H. Y. McSween Jr., S. M. Richardson, The composition of carbonaceous chondrite matrix. *Geochim. Cosmochim. Acta* **41**, 1145–1161 (1977). doi:10.1016/0016-7037(77)90110-7

26. M. C. De Sanctis, A. Raponi, E. Ammannito, M. Ciarniello, M. J. Toplis, H. Y. McSween, J. C. Castillo-Rogez, B. L. Ehlmann, F. G. Carrozzo, S. Marchi, F. Tosi, F. Zambon, F. Capaccioni, M. T. Capria, S. Fonte, M. Formisano, A. Frigeri, M. Giardino, A. Longobardo, G. Magni, E. Palomba, L. A. McFadden, C. M. Pieters, R. Jaumann, P. Schenk, R. Mugnuolo, C. A. Raymond, C. T. Russell, Bright carbonate deposits as evidence of aqueous alteration on (1) Ceres. *Nature* **536**, 54–57 (2016). doi:10.1038/nature18290 Medline

27. W. C. Feldman *et al*., Gamma-ray, neutron, and alpha-particle spectrometers for the Lunar Prospector mission. *J. Geophys. Res.* **109**, E07S06 (2004). doi:10.1029/2003JE002207

28. G. F. Knoll, *Radiation Detection and Measurement* (John Wiley & Sons, Inc., 1989).

29. T. H. Prettyman, "Dawn Gamma Ray and Neutron Detector raw Ceres counts V1.0," *DAWN-A-GRAND-2-EDR-CERES-COUNTS-V1.0*, https://pds.jpl.nasa.gov (NASA Planetary Data System, 2016).

30. T. H. Prettyman, N. Yamashita, "Dawn Gamma Ray and Neutron Detector calibrated Ceres counts V1.0," *DAWN-A-GRAND-3-RDR-CERES-COUNTS-V1.0*, https://pds.jpl.nasa.gov (NASA Planetary Data System, 2016).

31. D. J. Lawrence, P. N. Peplowski, T. H. Prettyman, W. C. Feldman, D. Bazell, D. W. Mittlefehldt, R. C. Reedy, N. Yamashita, Constraints on Vesta's elemental composition: Fast neutron measurements by Dawn's gamma ray and neutron detector. *Meteorit. Planet. Sci.* **48**, 2271–2288 (2013). doi:10.1111/maps.12187 Medline

32. N. Yamashita, T. H. Prettyman, D. W. Mittlefehldt, M. J. Toplis, T. J. McCoy, A. W. Beck, R. C. Reedy, W. C. Feldman, D. J. Lawrence, P. N. Peplowski, O. Forni, H. Mizzon, C. A. Raymond, C. T. Russell, Distribution of iron on Vesta. *Meteorit. Planet. Sci.* **48**, 2237–2251 (2013). doi:10.1111/maps.12139

33. T. H. Prettyman *et al*., Composition and structure of the martian surface at high southern latitudes from neutron spectroscopy. *J. Geophys. Res.* **109**, E05001 (2004). doi:10.1029/2003JE002139

34. D. B. Pelowitz, (Ed.), MCNPX User's Manual, Los Alamos National Laboratory document LA-CP-11-00438 (2011).

35. G. W. McKinney, D. J. Lawrence, T. H. Prettyman, R. C. Elphic, W. C. Feldman, J. J. Hagerty, MCNPX benchmark for cosmic ray interactions with the Moon. *J. Geophys. Res.* **111**, E06004 (2006). doi:10.1029/2005JE002551

36. Radiation Safety Information Computational Center (RSICC), Oak Ridge National Laboratory, https://rsicc.ornl.gov/.

37. I. G. Mitrofanov, M. T. Zuber, M. L. Litvak, W. V. Boynton, D. E. Smith, D. Drake, D. Hamara, A. S. Kozyrev, A. B. Sanin, C. Shinohara, R. S. Saunders, V. Tretyakov, CO_2 snow depth and subsurface water-ice abundance in the northern hemisphere of Mars. *Science* **300**, 2081–2084 (2003). doi:10.1126/science.1084350 Medline

38. W. V. Boynton, G. J. Taylor, L. G. Evans, R. C. Reedy, R. Starr, D. M. Janes, K. E. Kerry, D. M. Drake, K. J. Kim, R. M. S. Williams, M. K. Crombie, J. M. Dohm, V. Baker, A. E. Metzger, S. Karunatillake, J. M. Keller, H. E. Newsom, J. R. Arnold, J. Brückner, P. A. J. Englert, O. Gasnault, A. L. Sprague, I. Mitrofanov, S. W. Squyres, J. I. Trombka, L. d'Uston, H. Wänke, D. K. Hamara, Concentration of H, Si, Cl, K, Fe, and Th in the low- and mid-latitude regions of Mars. *J. Geophys. Res.* **112**, E12S99 (2007). doi:10.1029/2007JE002887

39. D. J. Lawrence, W. C. Feldman, J. O. Goldsten, S. Maurice, P. N. Peplowski, B. J. Anderson, D. Bazell, R. L. McNutt Jr., L. R. Nittler, T. H. Prettyman, D. J. Rodgers, S. C. Solomon, S. Z. Weider, Evidence for water ice near Mercury's north pole from MESSENGER Neutron Spectrometer measurements. *Science* **339**, 292–296 (2013). doi:10.1126/science.1229953 Medline

40. T. H. Prettyman, D. W. Mittlefehldt, N. Yamashita, A. W. Beck, W. C. Feldman, J. S. Hendricks, D. J. Lawrence, T. J. McCoy, H. Y. McSween, P. N. Peplowski, R. C. Reedy, M. J. Toplis, L. Le Corre, H. Mizzon, V. Reddy, T. N. Titus, C. A. Raymond, C. T. Russell, Neutron absorption constraints on the composition of 4 Vesta. *Meteorit. Planet. Sci.* **48**, 2211–2236 (2013). doi:10.1111/maps.12244

41. P. M. O'Neill, Badhwar–O'Neill 2010 galactic cosmic ray flux model—revised. *IEEE Trans. Nucl. Sci.* **6**, 3148–3153 (2010).

42. The Badhwar and O'Neill Galactic Cosmic Ray (GCR) model can be obtained by sending a request to patrick.m.oneill@nasa.gov.

43. T. H. Prettyman, "Dawn GRaND Ephemeris, Pointing, and Geometry, V2," *DAWN-A-GRAND-3-RDR-CERES-COUNTS-V1.0*, https://pds.jpl.nasa.gov (NASA Planetary Data System, 2016).

44. R. P. Gardner, K. Verghese, On the solid angle subtended by a circular disk. *Nucl. Instrum. Methods* **93**, 163–167 (1971). doi:10.1016/0029-554X(71)90155-8

45. M. H. Kalos, P. A. Whitlock, *Monte Carlo Methods, Volume I: Basics* (John Wiley & Sons, Inc., 1986).

46. D. W. Mittlefehldt, Asteroid (4) Vesta: I. The howardite-eucrite-diogenite (HED) clan of meteorites. *Chemie der Erde - Geochemistry* **75**, 155–183 (2015). doi:10.1016/j.chemer.2014.08.002

47. E. K. Jessberger, A. Christoforidis, J. Kissel, Aspects of the major element composition of Halley's dust. *Nature* **332**, 691–695 (1988). doi:10.1038/332691a0

48. W. C. Feldman, A. Pathare, S. Maurice, T. H. Prettyman, D. J. Lawrence, R. E. Milliken, B. J. Travis, Mars Odyssey neutron data: 2. Search for buried excess water ice deposits at nonpolar latitudes on Mars. *J. Geophys. Res.* **116**, E11009 (2011). doi:10.1029/2011JE003806

49. A. S. Rivkin, J.-Y. Li, R. E. Milliken, L. F. Lim, A. J. Lovell, B. E. Schmidt, L. A. McFadden, B. A. Cohen, The surface composition of Ceres. *Space Sci. Rev.* **163**, 95–116 (2010). doi:10.1007/s11214-010-9677-4

50. T. N. Titus, Ceres: Predictions for near-surface water ice stability and implications for plume generating processes. *Geophys. Res. Lett.* **42**, 2130–2136 (2015). doi:10.1002/2015GL063240

51. P. O. Hayne, O. Aharonson, Thermal stability of ice on Ceres with rough topography. *J. Geophys. Res. Planets* **120**, 1567–1584 (2015). doi:10.1002/2015JE004887

52. AstDyS-2 Asteroids Dynamic Site, http://hamilton.dm.unipi.it/astdys/index.php?pc=1.1.6&n=1, Retrieved 3 November 2016.

53. N. Schorghofer, The lifetime of ice on main belt asteroids. *Astrophys. J.* **682**, 697–705 (2008). doi:10.1086/588633

54. N. Schorghofer, Planetary-code-collection: Thermal and ice evolution models for planetary surfaces v1.1.1; https://github.com/nschorgh/Planetary-Code-Collection/; doi:10.5281/zenodo.48851 (2016).

55. A. W. Beck, D. J. Lawrence, P. N. Peplowski, T. H. Prettyman, T. J. McCoy, H. Y. McSween Jr., M. J. Toplis, N. Yamashita, Using HED meteorites to interpret neutron and gamma-ray data from asteroid 4 Vesta. *Meteorit. Planet. Sci.* **50**, 1311–1337 (2015). doi:10.1111/maps.12467

56. J. A. Cartwright, U. Ott, D. W. Mittlefehldt, J. S. Herrin, S. Herrmann, S. A. Mertzman, K. R. Mertzman, Z. X. Peng, J. E. Quinn, The quest for regolithic howardites. Part 1: Two trends uncovered using noble gases. *Geochim. Cosmochim. Acta* **105**, 395–421 (2013). doi:10.1016/j.gca.2012.11.047

57. J. A. Cartwright, U. Ott, D. W. Mittlefehldt, The quest for regolithic howardites. Part 2: Surface origins highlighted by noble gases. *Geochim. Cosmochim. Acta* **140**, 488–508 (2014). doi:10.1016/j.gca.2014.05.033

58. N. G. Lunning, K. C. Welten, H. Y. McSween Jr., M. W. Caffee, A. W. Beck, Grosvenor Mountains 95 howardite pairing group: Insights into the surface regolith of asteroid 4 Vesta. *Meteorit. Planet. Sci.* **51**, 167–194 (2016). doi:10.1111/maps.12580

59. R. Jaumann, D. A. Williams, D. L. Buczkowski, R. A. Yingst, F. Preusker, H. Hiesinger, N. Schmedemann, T. Kneissl, J. B. Vincent, D. T. Blewett, B. J. Buratti, U. Carsenty, B. W. Denevi, M. C. De Sanctis, W. B. Garry, H. U. Keller, E. Kersten, K. Krohn, J.-Y. Li, S. Marchi, K. D. Matz, T. B. McCord, H. Y. McSween, S. C. Mest, D. W. Mittlefehldt, S. Mottola, A. Nathues, G. Neukum, D. P. O'Brien, C. M. Pieters, T. H. Prettyman, C. A. Raymond, T. Roatsch, C. T. Russell, P. Schenk, B. E. Schmidt, F. Scholten, K. Stephan, M. V. Sykes, P. Tricarico, R. Wagner, M. T. Zuber, H. Sierks, Vesta's shape and morphology. *Science* **336**, 687–690 (2012). doi:10.1126/science.1219122 Medline

60. P. Schenk, D. P. O'Brien, S. Marchi, R. Gaskell, F. Preusker, T. Roatsch, R. Jaumann, D. Buczkowski, T. McCord, H. Y. McSween, D. Williams, A. Yingst, C. Raymond, C. Russell, The geologically recent giant impact basins at Vesta's south pole. *Science* **336**, 694–697 (2012). doi:10.1126/science.1223272 Medline

61. M. C. De Sanctis, J.-P. Combe, E. Ammannito, E. Palomba, A. Longobardo, T. B. McCord, S. Marchi, F. Capaccioni, M. T. Capria, D. W. Mittlefehldt, C. M. Pieters, J. Sunshine, F. Tosi, F. Zambon, F. Carraro, S. Fonte, A. Frigeri, G. Magni, C. A. Raymond, C. T. Russell, D. Turrini, Detection of widespread hydrated materials on Vesta by the VIR imaging spectrometer on board the Dawn mission. *Astrophys. J.* **758**, L36 (2012). doi:10.1088/2041-8205/758/2/L36

62. E. Fermi, *Nuclear Physics: A course given by Enrico Fermi at the University of Chicago. Notes compiled by Jay Orear, A. H. Rosenfeld, and R. A. Schluter* (The University of Chicago Press, Chicago, Illinois, ed. Revised Edition, 1950).

63. P. N. Peplowski, R. L. Klima, D. J. Lawrence, C. M. Ernst, B. W. Denevi, E. A. Frank, J. O. Goldsten, S. L. Murchie, L. R. Nittler, S. C. Solomon, Remote sensing evidence for an ancient carbon-bearing crust on Mercury. *Nat. Geosci.* **9**, 273–276 (2016). doi:10.1038/ngeo2669

64. R. C. Little, Latitude variation of the subsurface lunar temperature: Lunar Prospector thermal neutrons. *J. Geophys. Res.* **108**, 5046 (2003). doi:10.1029/2001JE001497

65. N. Yamashita, T. H. Prettyman, "Dawn's Gamma Ray and Neutron Detector: BGO Data Processing, Version 4.1," *DAWN-A-GRAND-3-RDR-CERES-COUNTS-V1.0*, https://pds.jpl.nasa.gov (NASA Planetary Data System, 2016).

66. R. C. Reedy, Planetary gamma-ray spectroscopy. *9th Lunar Planet. Sci. Conf.*, 2961-2984 (1978).

67. T. H. Prettyman, N. Yamashita, R. C. Reedy, H. Y. McSween Jr., D. W. Mittlefehldt, J. S. Hendricks, M. J. Toplis, Concentrations of potassium and thorium within Vesta's regolith. *Icarus* **259**, 39–52 (2015). doi:10.1016/j.icarus.2015.05.035

68. XCOM, Photon cross sections database, National Institute of Standards and Technology; http://physics.nist.gov/PhysRefData/Xcom/html/xcom1.html; Retrieved on 3 November 2016.

69. P. N. Peplowski, D. J. Lawrence, L. G. Evans, R. L. Klima, D. T. Blewett, J. O. Goldsten, S. L. Murchie, T. J. McCoy, L. R. Nittler, S. C. Solomon, R. D. Starr, S. Z. Weider, Constraints on the abundance of carbon in near-surface materials on Mercury: Results from the MESSENGER Gamma-Ray Spectrometer. *Planet. Space Sci.* **108**, 98–107 (2015). doi:10.1016/j.pss.2015.01.008

70. T. H. Prettyman, J. J. Hagerty, R. C. Elphic, W. C. Feldman, D. J. Lawrence, G. W. McKinney, D. T. Vaniman, Elemental composition of the lunar surface: Analysis of gamma ray spectroscopy data from Lunar Prospector. *J. Geophys. Res.* **111**, E12007 (2006). doi:10.1029/2005JE002656

71. C. M. O'D. Alexander, K. T. Howard, R. Bowden, M. L. Fogel, The classification of CM and CR chondrites using bulk H, C and N abundances and isotopic compositions. *Geochim. Cosmochim. Acta* **123**, 244–260 (2013). doi:10.1016/j.gca.2013.05.019

72. A. Garenne, P. Beck, G. Montes-Hernandez, R. Chiriac, F. Toche, E. Quirico, L. Bonal, B. Schmitt, The abundance and stability of "water" in type 1 and 2 carbonaceous chondrites (CI, CM and CR). *Geochim. Cosmochim. Acta* **137**, 93–112 (2014). doi:10.1016/j.gca.2014.03.034

73. A. J. King, J. R. Solomon, P. F. Schofield, S. S. Russell, Characterising the CI and CI-like carbonaceous chondrites using thermogravimetric analysis and infrared spectroscopy. *Earth Planets Space* **67**, 198 (2015). doi:10.1186/s40623-015-0370-4

74. A. E. Rubin, Mineralogy of meteorite groups. *Meteorit. Planet. Sci.* **32**, 231–247 (1997). doi:10.1111/j.1945-5100.1997.tb01262.x

75. K. Tomeoka, P. R. Buseck, Matrix mineralogy of the Orgueil CI carbonaceous chondrite. *Geochim. Cosmochim. Acta* **52**, 1627–1640 (1988). doi:10.1016/0016-7037(88)90231-1

76. A. P. Zent, D. J. Howard, R. C. Quinn, H_2O adsorption on smectites: Application to the diurnal variation of H_2O in the Martian atmosphere. *J. Geophys. Res. Planets* **106**, 14667–14674 (2001). doi:10.1029/2000JE001394

77. T. B. McCord, T. M. Orlando, G. Teeter, G. B. Hansen, M. T. Sieger, N. G. Petrik, L. Van Keulen, Thermal and radiation stability of the hydrated salt minerals epsomite, mirabilite, and natron under Europa environmental conditions. *J. Geophys. Res. Planets* **106**, 3311–3319 (2001). doi:10.1029/2000JE001282

78. C. M. O'D. Alexander, R. Bowden, M. L. Fogel, K. T. Howard, Carbonate abundances and isotopic compositions in chondrites. *Meteorit. Planet. Sci.* **50**, 810–833 (2015). doi:10.1111/maps.12410

79. A. R. Hendrix, F. Vilas, J.-Y. Li, The UV signature of carbon in the solar system. *Meteorit. Planet. Sci.* **51**, 105–115 (2016). doi:10.1111/maps.12575

80. E. J. Zeller, L. B. Ronca, Space weathering of lunar and asteroidal surfaces. *Icarus* **7**, 372–379 (1967). doi:10.1016/0019-1035(67)90082-6

81. S. Marchi, A. I. Ermakov, C. A. Raymond, R. R. Fu, D. P. O'Brien, M. T. Bland, E. Ammannito, M. C. De Sanctis, T. Bowling, P. Schenk, J. E. C. Scully, D. L. Buczkowski, D. A. Williams, H. Hiesinger, C. T. Russell, The missing large impact craters on Ceres. *Nat. Commun.* **7**, 12257 (2016). doi:10.1038/ncomms12257 Medline

82. R. T. Daly, P. H. Schultz, Predictions for impactor contamination on Ceres based on hypervelocity impact experiments. *Geophys. Res. Lett.* **42**, 7890–7898 (2015). doi:10.1002/2015GL065601

83. W. C. Feldman, D. J. Lawrence, R. C. Elphic, D. T. Vaniman, D. R. Thomsen, B. L. Barraclough, S. Maurice, A. B. Binder, Chemical information content of lunar thermal and epithermal neutrons. *J. Geophys. Res.* **105**, 20347–20363 (2000). doi:10.1029/1999JE001183

84. D. Wolf, H. Palme, The solar system abundances of phosphorus and titanium and the nebular volatility of phosphorus. *Meteorit. Planet. Sci.* **36**, 559–571 (2001). doi:10.1111/j.1945-5100.2001.tb01897.x

85. E. Jarosewich, Chemical analyses of meteorites at the Smithsonian Institution: An update. *Meteorit. Planet. Sci.* **41**, 1381–1382 (2006). doi:10.1111/j.1945-5100.2006.tb00528.x

86. A. E. Rubin, J. M. Trigo-Rodríguez, H. Huber, J. T. Wasson, Progressive aqueous alteration of CM carbonaceous chondrites. *Geochim. Cosmochim. Acta* **71**, 2361–2382 (2007). doi:10.1016/j.gca.2007.02.008

87. E. Jarosewich, Chemical analyses of meteorites: A compilation of stony and iron meteorite analyses. *Meteoritics* **25**, 323–337 (1990). doi:10.1111/j.1945-5100.1990.tb00717.x

88. H. B. Wiik, On regular discontinuities in the composition of meteorites. *Societas Scientarium Fennica. Comment. Phys.-Math.* **34**, 135–145 (1969).

89. H. B. Wiik, The chemical composition of some stony meteorites. *Geochim. Cosmochim. Acta* **9**, 279–289 (1956). doi:10.1016/0016-7037(56)90028-X